Analysis of flame propagation mechanisms during light-round in an annular spray flame combustor: the impact of wall heat transfer and two-phase flow

Karl Töpperwien, Stefano Puggelli, Ronan Vicquelin

Analysis of flame propagation mechanisms during light-round in an annular spray flame combustor: the impact of wall heat transfer and two-phase flow

Karl Töpperwien[a,*], Stefano Puggelli[a,1], Ronan Vicquelin[a]

[a] *Laboratoire EM2C, CNRS, CentraleSupélec, Université Paris-Saclay, 8 - 10 Rue Joliot Curie, 91192, Gif-sur-Yvette cedex, France*

Abstract

Ignition in annular multi-burner combustors is marked by a succession of four phases, ending with a characteristic flame expansion from burner to burner, often referred to as light-round. During this last phase, flame propagation is prone to substantial change depending on the boundary and operating conditions. With realistic aero-engine conditions in mind, wall heat transfers can be enhanced during ignition in cold wall conditions, which aid an understanding of the main governing mechanisms of flame propagation. From a modeling perspective, several works have outlined the need for detailed descriptions of the liquid phase, turbulent combustion and wall heat transfer, which are all included in the present work for the first time. Large-Eddy Simulations of light-round are performed in the annular MICCA-Spray combustor with cold walls, Lagrangian particle tracking, a dynamic closure for the sub-grid scale flame surface wrinkling as well as a custom tabulated wall

*Corresponding author: karl.topperwien@centralesupelec.fr
[1]Present address: SAFRAN Tech, Rue des Jeunes Bois, Châteaufort - CS 80112, Magny-les-Hameaux 78772, France

model. The predicted light-round duration from the simulation is found to be in good agreement with experimental data. It is shown that the volumetric expansion of burnt gases induces a flow acceleration in azimuthal direction which constitutes the main driving mechanism of flame propagation. Droplet accumulations in the wake of swirling jets are generated ahead of the propagating flame fronts, which in turn cause a characteristic sawtooth propagation mode of the leading point. A cooling effect of the combustor walls on burnt gases is particularly pronounced downstream, diminishing the resulting flame propagation speed. The main governing mechanisms are investigated by means of a mathematical model for the absolute turbulent flame speed to quantify their relative impact on flame propagation. Finally, *a priori* estimations are provided for the flame propagation speed based on different models and boundary conditions, which are directly plugged into the model.
Keywords: light-round; annular combustor; ignition; spray flames; dynamic modeling

---

1. Introduction

Light-round constitutes the final phase in a complex four-step process of forced ignition in annular combustion chambers [1, 2]. After a spark is generated in phase I, and the initial flame kernel has grown (phase II) to establish a full-scale ignition of the first burner (phase III), a burner-to-burner flame propagation can eventually be observed (phase IV) referred to as light-round [2].

A multi-burner configuration is thus required to characterize this final

phase which strongly depends on combustor design and operating conditions. Studies can be found in the literature focusing on linear burner arrays observing distinct patterns for premixed (spanwise, axial and hybrid) [3, 4] and non-premixed (propagation along flammable bridges) [5] setups. These are different from patterns with liquid fuel injection systems which exhibit a branch propagation across neighboring spray branches or an arch-like propagation [6, 7]. Marrero-Santiago et al. [7] also note that the arch propagation mode substantially increases the ignition delay time. All works cite injector spacing as an influential parameter controlling the resulting pattern or causing the pattern to switch.

While linear burner arrays provide detailed insights into the flame spreading process, they lack key features of industrial annular combustors (e.g. flame propagation as arch, flame front merging). Lab-scale representations of annular designs—the subject of the present work—have emerged with first experimental studies by Bourgouin et al. [8], revealing the flame's distinct arch shape. Interestingly, Machover et al. [9] report a sawtooth movement from burner to burner in their 12-burner premixed bluff-body configuration. More recent works also outline an effect of common ignition modes "Spark First, Fuel Later" (SFFL) and "Fuel First, Spark Later" (FFSL) [10], bulk flow velocity and equivalence ratio [11] on the observed propagation pattern.

Beyond propagation patterns, the propagation speed and the resulting light-round duration are subject to extensive research as well and are found to be controlled by (i) burnt gas expansion, (ii) the laminar flame speed and (iii) wall heat transfer (among others). The volumetric expansion of burnt gases in the chamber constitutes a key mechanism [8, 9] governing the flow

acceleration in azimuthal direction, which is proportional to the density ratio of fresh and burnt gases (ρ_u/ρ_b).

The injector velocity is yet another driving mechanism inversely proportional to the measured light-round duration [8, 12–15]. This relation is investigated by Machover et al. [9] in a premixed annular combustor featuring 12 or 18 bluff-body burners. The authors note that adding swirl, or increasing the equivalence ratio, increases the flame propagation speed, leading to shorter light-round durations. Interestingly though, the impact of flow velocity on the light-round duration is less pronounced for non-premixed operating conditions [16]. In turn, bulk flow velocity (precisely its circumferential component) becomes the main governing effect of flame propagation in the particular case of oblique injectors [17]. As for linear setups, the same behavior in terms of flame propagation speed is reproduced in annular chambers when the inter-burner spacing is varied [9, 16].

The laminar flame speed should also be mentioned as an influential parameter for flame propagation. In the context of liquid fuels, detailed insights were initially gained from academic cases. Laminar flame speeds in droplet mists for overall lean conditions are generally lower than the gaseous laminar flame speed at the same equivalence ratio, suggesting that spray flames propagate at a leaner equivalence ratio than the overall equivalence ratio [18–20]. Such trends are confirmed by Prieur et al. [21] who have carried out ignition experiments in the swirled annular combustor MICCA-Spray, with different liquid fuels and compared the data with premixed gaseous fuels. While the flame shapes remain comparable for all cases, liquid fuels generally tend to increase the light-round duration, depending on the fuel volatility. This im-

plies that flame propagation speeds are lower than in the equivalent gaseous case.

More recently, similar studies were performed by Ciardiello et al. [15] for different gaseous fuels. Given a matched laminar flame speed, fixed bulk velocity and spark location, but otherwise variable parameters (fuel type, equivalence ratio, thermal power), the light-round duration of two setups is essentially constant. The authors conclude that the laminar flame speed has a first order impact on the resulting flame propagation speed during light-round.

Furthermore, the rate of burnt gas dilatation is characterized on a fundamental level for flame propagation in droplet mists and appears to be influenced by turbulence, initial droplet diameter and liquid equivalence ratio [22, 23] (*i.e.* the contribution of *liquid* fuel to the gaseous carrier phase).

Data on light-round durations for pre-heated and cold combustor walls have been reported in [14, 24]. At constant bulk flow velocity, pre-heating the combustor walls drastically reduces the light-round duration by $50-70\%$, suggesting that combustor wall temperatures are crucial for the understanding of flame propagation.

Large-Eddy Simulations have proven to be a reliable tool in order to study light-rounds numerically after first pioneering works by Boileau et al. [25] giving rise to further research with gaseous [14, 26, 27] and liquid fuels [28–30]. Most of these numerical studies rely on a simplified combustion chemistry to limit the computational costs of LES, and the thickened flame model (TFLES [31, 32]). A tabulated chemistry approach based on filtered flamelets (F-TACLES [33]) was shown to perform similarly to TFLES [26].

Detailed kinetics have been included directly in [27] considering each cell as a perfectly stirred reactor. In terms of the liquid phase description, both monodisperse Euler-Euler (EE) [30] as well as polydisperse Euler-Lagrange (EL) [29] simulations of light-round were performed.

While LES is generally able to describe and qualitatively retrieve the light-round driving mechanisms observed experimentally, the results are quantitatively sensitive to the modeling choices. Detailed numerical models can improve the accuracy of the predicted light-round duration in LES, as separately highlighted and quantified by the following studies:

- The effect of dynamic combustion modeling has been investigated by Puggelli et al. [34]. The authors proved that a constant ("static") flame surface wrinkling parameter β cannot be justified from a physical standpoint given the heterogeneity of the β field revealed by a dynamic evaluation of said parameter. Despite worse results in terms of the observed light-round duration (increase by 20% over a constant β approach), the argument for a dynamic combustion model is still upheld. A cancellation of errors originating from *other* modeling choices is cited as principal reason for such discrepancy. This error cancellation was more unfavorable (and more pronounced) in the case of the dynamic approach, while hidden (by coincidence) in the constant β case.

- An appropriate description of the liquid phase appears to be essential, in particular the inherent polydispersion of the fuel droplets, resulting from the fuel injection characteristics, droplet evaporation and the flow field. A polydisperse Euler-Lagrange approach similar to [29] should

then be favored over previous monodisperse Euler-Euler computations of light-round with liquid fuel [28, 30, 34].

- Puggelli et al. [24] have demonstrated in an *a priori* study the intricate relation between variable thermodynamic properties of the boundary layer and the resulting wall heat fluxes. Their work postulated that detailed modeling of wall heat transfers would prove to be crucial in those cases in which hot burnt gases are in contact with cold combustor walls.

All these numerical works have anticipated or even proven an impact on light-round duration and thus the flame propagation speed, intentionally limiting their modeling changes to one aspect per case. Despite this, no study has to date included *all* these findings in light-round simulations for a comprehensive *a posteriori* analysis of the governing mechanisms of flame propagation during light-round.

The goal of this work is therefore threefold: our objective is first to characterize the main governing mechanisms during light-round with liquid fuels and cold (*i.e.* $T_w = 300\,\mathrm{K}$) combustor walls by means of LES. For the first time detailed numerical models recently identified in the literature are combined establishing a new baseline case different from previous works: dynamic combustion modeling, polydisperse Euler-Lagrange formalism and advanced wall-modeling. The cold-wall case enhances the effect of wall heat transfer. It is therefore the subject of the present study. Such conditions are not only relevant for engine start-up, but also for high-altitude relight where inlet air temperatures can be as low as 238 K at 30 000 ft (9144 m) of altitude and cool the engine substantially. Our operating conditions (detailed

later) admittedly represent an idealization of real engine conditions, but can still be considered as a first step towards characterizing heat transfer during light-round. We also note that only a few studies exist to date in the open literature which are concerned with emulating realistic high altitude relight scenarios in terms of low temperatures *and* low pressures [35–39].

For an *a posteriori* quantification of heat loss effects a complementary adiabatic case is included.

Second, a mathematical low-order model for turbulent flame propagation during light-round is derived. Links are established between the governing mechanisms and the expressions in the model on which they act. Ultimately, flame speeds are estimated for different modeling assumptions, which are plugged into the model to assess their respective effect on the flame propagation speed.

The study is organized as follows: a brief overview of the combustor geometry is given in Sec. 2, followed by details on the numerical setup in Sec. 3, in particular the custom approach to compute wall heat transfers, the liquid phase description and the dynamic combustion model. Results are presented in Sec. 4 focusing on the driving mechanisms of flame propagation. The aspect regarding the low-order model, its relationship with the driving mechanisms and the impact of modeling choices is finally addressed in Sec. 5.

2. Experimental configuration

The MICCA-Spray combustor (Fig. 1(a)) is a test rig at the EM2C laboratory [21, 40] designed to perform experiments in an annular combustion chamber. It features sixteen swirled spray injectors arranged in an annular

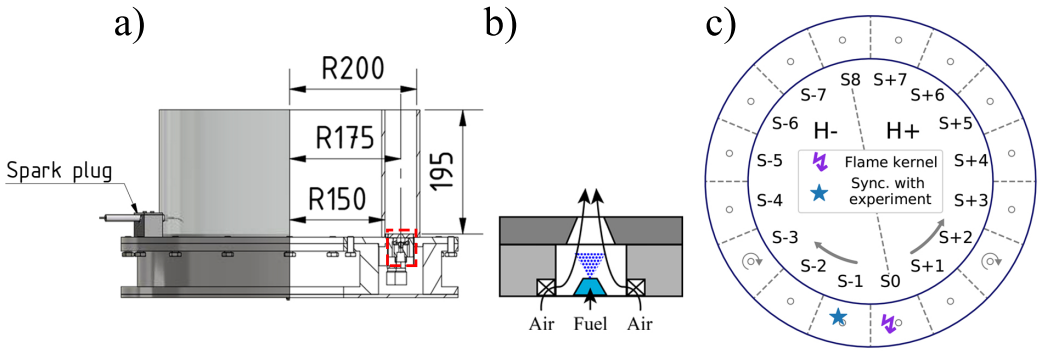

Figure 1: a) Setup of the MICCA-Spray test rig at the EM2C laboratory [21, 40]. A simplified sketch of the injector assembly marked by the dashed rectangle is given in Fig. b). Figure c) shows the sector numbering, the flame propagation directions in each half of the chamber (thick arrows) and the swirl orientation (thin arrows). The spark plug is mounted in sector $S0$. The ignition of sector S-1 is used as reference to compare experimental and numerical light-round durations. (All dimensions in millimeters.)

fashion at a radius of $R = 0.175\,\mathrm{m}$. Each injector assembly consists of a swirler, a concentrically mounted atomizer and a terminal plate with an integrated nozzle and an outlet diameter of $d_{inj} = 8\,\mathrm{mm}$ (see Fig. 1(b)). The atomizer is recessed by 5 mm relative to the nozzle outlet allowing the hollow-cone fuel spray to partially interact with the nozzle walls and improve the atomization process. The combustion chamber is confined by two concentric quartz tubes with dimensions $R_{in} = 0.15\,\mathrm{m}$, $R_{out} = 0.20\,\mathrm{m}$ and $h = 0.195\,\mathrm{m}$ which allow for optical access (Fig. 1(a)). The chamber is operated at ambient pressure and a global equivalence ratio $\phi_{glob} = 0.89$, corresponding to a nominal thermal power output $\mathcal{P}_{th} = 79.3\,\mathrm{kW}$ under steady-state operating conditions. Ignition is triggered by an electrical spark plug in sector $S0$ relative to which the chamber is divided into a positive (H+) and negative (H-) half (Fig. 1(c)). After successful ignition of the entire combustor, the fuel

supply is immediately cut to extinguish all flames. The target wall temperature of $T_w = 300\,\mathrm{K}$ is reestablished at the start of each run after a cool-down time of at least ten minutes. Pre-fueling is initiated for the subsequent run for a few seconds after which the spark plug is retriggered to perform the next ignition event.

Since the experimental setup is already covered in previous publications, the interested reader is directly referred to [21, 40] for more details on the experimental diagnostics and the available dataset.

3. Numerical setup

In light of recent numerical works on light-round ignition, the present work aims at including the previous individual findings in one *single* numerical setup. Its key elements are briefly summarized here and more details are provided for the tabulated wall model.

Large-Eddy Simulations are performed with the AVBP solver [41] developed by CERFACS. The separate treatment for the gas and liquid phase is described in the following subsections.

3.1. Gas phase

The three-dimensional, filtered, compressible, reactive Navier-Stokes equations are solved on an unstructured tetrahedral grid using the Two-step Taylor-Galerkin Centered scheme (TTGC) [42] with third-order accuracy in space and time (for arbitrary meshes). Subgrid-scale contributions are computed following the classical eddy viscosity assumption. The turbulent eddy viscosity is evaluated according to the SIGMA model [43]. The turbulent

species diffusivity and the turbulent heat conduction coefficient are determined from the turbulent Schmidt (Sc_t) and Prandtl (Pr_t) numbers (both equal to 0.6).

3.2. Dispersed phase

Assuming spherical fuel droplets and a dilute spray, the fundamental equations for droplet motion in a Lagrangian framework employed in this work are given as:

$$\frac{dx_{p,i}}{dt} = u_{p,i} \tag{1}$$

$$\frac{du_{p,i}}{dt} = \frac{f_{p,i}}{m_{p,i}} \tag{2}$$

$$\frac{dm_{p,i}}{dt} = \dot{m}_{p,i} \tag{3}$$

$$\frac{dC_{p,l}T_{p,i}}{dt} = \frac{1}{m_{p,i}}\left(-\phi^c_{g,i} + \dot{m}_{p,i}L_v(T_{p,i})\right) \tag{4}$$

with $x_{p,i}$, $u_{p,i}$, $m_{p,i}$ and $T_{p,i}$ denoting the droplet position, velocity, mass and temperature of the ith droplet. For the remainder of this work, indexing of droplets is omitted. $C_{p,l}$ is the liquid heat capacity which may vary with temperature. The droplet density is set constant ($\rho_l = 688\,\mathrm{kg/m^3}$). External forces acting on the droplets are included in f_p and are limited to drag force within this study, following the Schiller-Naumann drag force model [44]. Additional terms appear due to heat and mass transfer between the phases with the evaporation rate $\dot{m}_p$ and gaseous conductive heat fluxes ϕ^c_g at the droplet surface given as:

$$\dot{m}_p = -\pi d_p \mathrm{Sh} \rho_g D_g \ln\left(1 + B_M\right) \tag{5}$$

$$\phi^c_g = -\pi d_p \mathrm{Nu} \lambda \left(T_\infty - T_p\right) \frac{\ln\left(1 + B_T\right)}{B_T} \tag{6}$$

where d_p, Sh, ρ_g, D_g, Nu and λ denote droplet diameter, the Sherwood number, the density of the gaseous mixture, the diffusion coefficient of the gas phase, the Nusselt number, and the thermal conductivity in the gas phase.

These equations represent the Spalding model [45] with corrections proposed by Abramzon and Sirignano [46] to account for the presence of vapor films around evaporating droplets modifying the mass and thermal transport. This affects in particular the evaluation of the Spalding numbers of mass and thermal transport, B_M and B_T. Assuming thermodynamic equilibrium, B_M can be evaluated when the saturation pressure at the droplet surface is known, which is computed from the pretabulated Clausius-Clapeyron formula. Sherwood and Nusselt numbers, which appear in the correction of Abramzon and Sirignano [46], follow a correlation proposed by Frössling [47] and are functions of the droplet Reynolds number Re_p, the Prandtl number $\mathrm{Pr}_{\mathrm{film}}$ and the Schmidt number $\mathrm{Sc}_{\mathrm{film}}$ in the vapor film. The thermal conductivity of the film is given by $\lambda = \mu C_{p,g}/\mathrm{Pr}_{\mathrm{film}}$, where μ and $C_{p,g}$ denote the gaseous viscosity and heat capacity in the film. These film properties are evaluated at a reference state, which can be interpolated between far-field and droplet surface conditions using the "third-rule" [48]. $\mathrm{Pr}_{\mathrm{film}}$ and $\mathrm{Sc}_{\mathrm{film}}$ are functions of the film temperature and film mixture fraction. Those dimensionless quantities are evaluated from a polynomial fit validated in [49]. Ultimately, the latent heat of vaporization at the droplet temperature L_v is read from lookup tables.

The governing equations are solved using a two-step Runge-Kutta scheme and coupled at every iteration to the gas-phase solver. We point out that the

dilute spray assumption (liquid volume fraction in the range of $10^{-6} \leq \alpha_l \leq 10^{-3}$ as defined *e.g.,* in [50]) can be justified further away from the injector where droplet interactions become less relevant [51]. They are neglected here in favor of modeling the processes of interest such as dispersion, evaporation, fuel/air mixing or combustion whilst keeping the computational efforts affordable.

3.2.1. Fuel injection model

A fully atomized, hollow-cone fuel spray is generated by the phenomenological FIM-UR model (fuel injection method by upstream reconstruction) [52, 53] and injected at the tip of each of the sixteen atomizers. The injected droplet distribution is a result of a calibration based on PDA measurements in non-reacting conditions performed at a height of $x = 5\,\mathrm{mm}$ from the combustor backplane and a radius of $r = 5\,\mathrm{mm}$ from the axis of rotation (cf. filled histogram in Fig. 2). This experimentally measured distribution is evaporation-corrected to account for the fact that droplets may evaporate and thus decrease in size during their path from the atomizer to the measurement position. For this correction, a constant value of the d^2-law coefficient $\lambda_{d2} = 1.65 \times 10^{-8}\,\mathrm{m^2 s^{-1}}$ is derived from Ref. [54]. An average time-of-flight (TOF) is computed from separate LES and is given as $\tau_{\mathrm{TOF}} = 1.2\,\mathrm{ms}$. Both parameters ($\lambda_{d2}$ and τ_{TOF}) are then applied to all bins of the experimental droplet distribution, yielding the corrected distribution from which the injection diameter is sampled during LES. The remaining model parameters are set to $\theta = 26°$ and $\delta\theta = 6°$ (injection angle and deviation angle) and an injection velocity of $u_d = 10\,\mathrm{m/s}$ is applied for all droplet sizes at the moment of their generation.

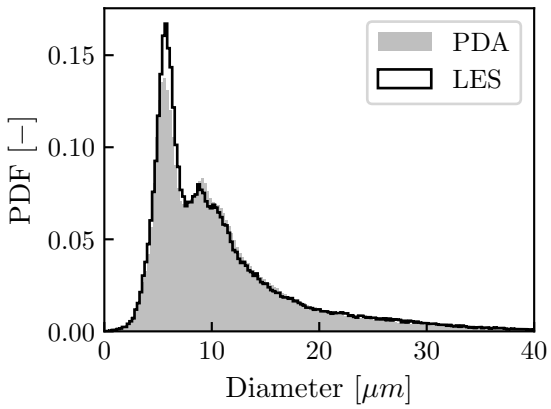

Figure 2: Droplet diameter distribution measured experimentally by PDA (before evaporation correction) and sampled in precursor LES at a radius of $r = 5\,\text{mm}$ from the axis of rotation and $x = 5\,\text{mm}$ above the chamber backplane. Experimental data kindly provided by G. Vignat based on the methodology described in [53] and applied to the same burner.

With these parameters, the histogram labeled "LES" in Fig. 2 is obtained from the calibration LES at the same position as in the PDA measurements.

It should be noted that each numerical droplet represents one physical droplet over the entire simulation. Secondary atomization is not taken into account.

3.3. Reaction kinetics and dynamic combustion model

Reaction kinetics are based on a global two-step scheme for n-heptane/air mixtures containing 6 species (C_7H_{16}, CO_2, CO, H_2O, O_2, N_2) [55]. Reaction rates are computed from the Arrhenius law with adjusted pre-exponential factors depending on the local equivalence ratio [56], requiring a unitary Lewis number assumption (Le = 1). A validation against detailed schemes [57] performed in [55] shows a reasonably good prediction of the unstrained laminar

burning velocity at ambient pressure and over a wide range of equivalence ratios. We note that the unity Lewis number assumption renders the two-step reaction mechanism virtually insensitive to strain. As discussed later, such simplification is acceptable for the description of flame front propagation during light-round. It should also be emphasized that auto-ignition or pyrolysis effects are very unlikely to occur with cold combustor walls ($T_w = 300\,\mathrm{K}$), justifying the use of reduced chemical reaction schemes.

Since cell sizes are not sufficiently small to fully resolve the flame on the numerical grid, artificial thickening (TFLES) is applied [31, 32], ensuring correct laminar flame burning velocity retrieval. The amount of local thickening by a factor $\mathcal{F}$ depends on the local cell size, the laminar flame thickness, and the number of prescribed grid points to resolve the flame profile (7 points used here). A flame sensor [32] combined with the evaluation of the local Takeno flame index [58] limits the thickening procedure to the premixed reaction zone only. As a consequence of the two-phase flow configuration, thickening is also applied to drag and evaporation [55]. The interested reader may find additional justification for the use of the TFLES model and the flame sensor in two-phase flows in Appendix A.

Interactions between strain effects and a thickened flame may result in a modified Damköhler number [31]. Strain-correction models exist for *laminar* flames developed by Popp et al. [59] which correct the laminar flame speed at elevated thickening factors. For the present investigations of turbulent flame propagation, no specific treatment is currently employed, but would be worth developing in future works. The two-step reaction mechanism thus predicts laminar flame speed values close to S_l^0 of unstrained flames for a

given equivalence ratio, even at elevated thickening values.

Furthermore, the thickened flame approach requires the flame surface to be corrected for unresolved sub-grid scale wrinkling effects, which may be described with a flame surface wrinkling model. Following the work of Charlette et al. [60], the flame surface wrinkling factor is expressed as:

$$\Xi_{\Delta} = \left(\frac{\Delta}{\delta_l}\right)^{\beta} \tag{7}$$

where Δ corresponds to the local mesh size, δ_l to the laminar flame thickness and β to a free parameter. As highlighted in [34], a dynamic evaluation of the β-parameter is recommended to account for different amounts of wrinkling of the propagating flame fronts on one hand, and stabilized flames downstream of these flame fronts on the other hand. Essentially, the wrinkling parameter β is determined following the work of Mouriaux et al. [61], using the same parameter set as in [34] with the exception of a higher update frequency (every 250 iterations).

3.4. Wall modeling

When wall-resolved LES is not an option, the near wall flow may be described with wall models. Wall boundary profiles can then be computed from algebraic models for example, which in turn require a certain set of assumptions to hold true.

As stated in [24], an algebraic wall law inevitably falls short of correctly predicting wall heat fluxes, even if density variations are included as in [62], since other properties (c_p, μ, λ) can vary substantially in the boundary layer. Puggelli et al. [24] have estimated an up to 70% lower heat flux under light-round conditions when standard algebraic wall models are used. Hence, in

an attempt to improve the modeling of the near wall flow in the burnt gas region, a tabulated wall model approach is proposed here.

Similar to the work of Maheu et al. [63], an interpolation database is generated to compute local wall heat fluxes and wall shear stresses as a function of known quantities at the first *off-wall* node of the mesh, also referred to as matching point. This approach appears to be a promising alternative to algebraic wall models.

Essentially, the one-dimensional Thin Boundary Layer Equations (TBLE) [64] are solved for a range of boundary conditions. The eddy viscosity μ_t is approximated according to the expression proposed by Cabot and Moin [65]:

$$\mu_t = \overline{\rho}\kappa y u_\tau^\star \left[1 - exp\left(-\frac{y^\star}{A^+}\right)\right]^2 \tag{8}$$

where κ is the von Kármán constant, y the wall distance, $u_\tau^\star$ the friction velocity, $y^\star$ the normalized wall distance and A^+ a parameter. Superscripted stars denote semi-local scaling [66, 67] of the friction velocity $u_\tau^\star = (\tau_w/\overline{\rho})^{0.5}$ and the normalized wall distance $y^\star = \overline{\rho} y u_\tau^\star/\overline{\mu}$ which is generally employed for variable property flows. The turbulent Prandtl number Pr_t appearing in the Thin Boundary Layer Equations is computed according to the formula of Kays [68].

The resulting wall heat fluxes and wall shear stresses obtained from TBLE are tabulated as a function of three parameters: the temperature T_{MP}, the velocity u_{MP} and the distance δ_{MP} of the matching point (subscript "MP", see sketch in Fig. 3). These parameters constitute the inputs for the interpolation routine during LES, with a value range predetermined from precursor simulations. To safely cover the entire range of possible combinations which may be encountered during light-round, T_{MP} is swept between $[350, 2300]\,\mathrm{K}$

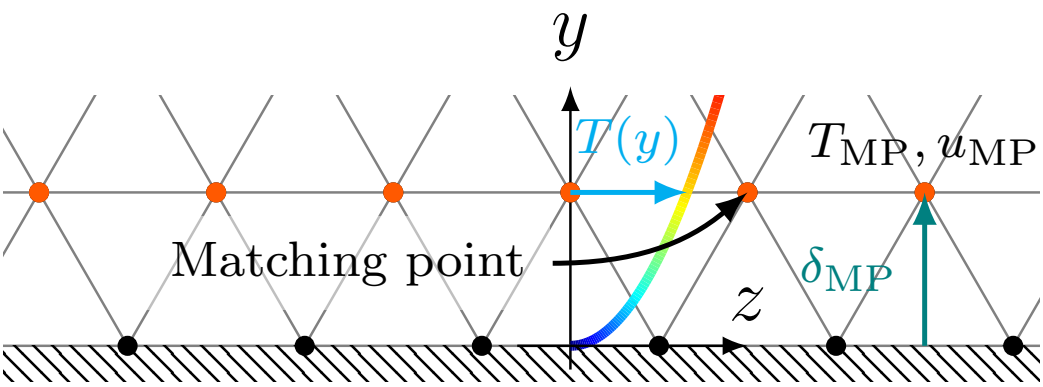

Figure 3: Illustration of matching points (red off-wall nodes) providing the input variables for the tabulated wall model. Wall nodes have a constant wall temperature of $T_w = 300\,\mathrm{K}$.

in steps of 50 K, u_{MP} between $[0.5, 50]\,\mathrm{ms}^{-1}$ in steps of $0.5\,\mathrm{ms}^{-1}$ and δ_{MP} between $[0.2, 1]\,\mathrm{mm}$ in steps of 0.01 mm. At $y = 0$ (*i.e.* at the wall), the boundary condition is set to $T = 300\,\mathrm{K}$ to solve the TBLE. For table generation, a theoretical burnt gas composition is imposed being equal to the global equivalence ratio, at which the combustor is operated ($\phi_{glob} = 0.89$) since variable compositions have not been considered in the generated database. The entire interpolation database comprises 324 000 data points for each target variable (wall heat flux and wall shear stress). This database is created only once and is then accessed by the LES code at each iteration to compute the corresponding wall heat fluxes and wall shear stresses by simple table interpolation at each matching point based on its current input parameters.

In order to ensure that the tabulated wall model is only applied in the burnt gas region, the off-wall progress variable c_{MP} is introduced to toggle between the tabulated wall model (for $c_{\mathrm{MP}} \geq 0.5$) and the standard algebraic wall model (otherwise), as the TBLE have not been solved for a fresh gas

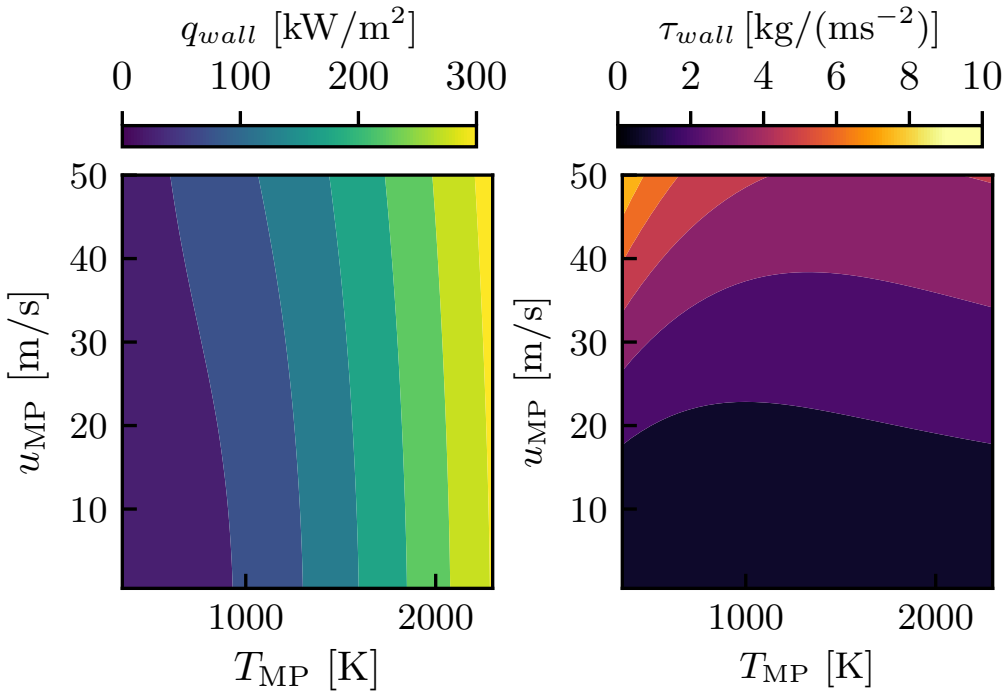

Figure 4: Tabulated wall heat flux q_{wall} and wall shear stress τ_{wall} at an arbitrarily chosen matching point distance $\delta_{\mathrm{MP}} = 0.4\,\mathrm{mm}$.

composition where variable-property effects with temperature are absent.

The three-dimensional parameter space is cut at an arbitrary matching point distance $\delta_{\mathrm{MP}} = 0.4\,\mathrm{mm}$ for visualization purposes and plotted in Fig. 4 as a two-dimensional cut-plane showing the evolution of q_{wall} and τ_{wall}. At constant δ_{MP}, the wall heat flux mainly increases with increasing matching point temperature T_{MP}, implying an increasing temperature difference between the matching point and the wall at $T_w = 300\,\mathrm{K}$. τ_{wall} is instead dominated by the matching point velocity u_{MP}.

For an assessment of the interpolation accuracy, random tuples of T_{MP}, u_{MP} and δ_{MP} are generated within the database limits and used to solve the

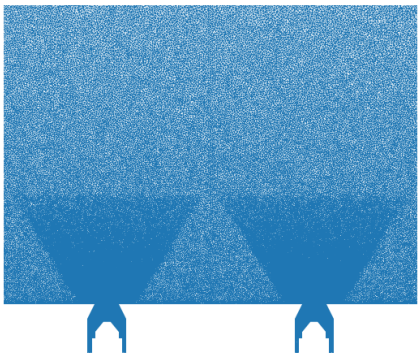

Figure 5: Azimuthal mesh cut of two adjacent sectors at $R = 0.175\,\mathrm{mm}$ transformed into a rectangular system.

TBLE. Comparing the resulting wall heat flux and wall shear stress with the interpolated values from the database using the *same* tuple yields a relative error below 1% for either target variable.

3.5. Numerical domain and boundary conditions

Figure 5 shows a mesh cut at $R = 0.175\,\mathrm{m}$ of the lower part of the combustion chamber clipped to two injectors. The full three-dimensional numerical domain (see Fig. 1) comprises the air plenum, all 16 injector assemblies and the entire combustion chamber. For numerical reasons, the upper part of the combustion chamber is immersed in a larger cylinder representing the atmosphere around the combustor (not shown in Fig. 1(a)) and extends 60 cm beyond the chamber outlet. The inclusion of the atmosphere is particularly advantageous, since it allows to impose the outlet boundary condition (ambient pressure) as far away from the *combustor outlet* as possible and also avoids interactions with the flame. Typical mesh sizes in the flame region are of the order of 0.2 mm (at the combustor backplane) to 0.5 mm (at a height

of 35 mm above the combustor backplane). The entire mesh contains 320 M thetrahedral cells.

For inlets and outlets, the Navier–Stokes characteristic boundary conditions [69] are applied. Mass flow rates are imposed at the air inlet ($\dot{m}_{air} = 30.2083\,\mathrm{g/s}$) and at each of the fuel inlets ($\dot{m}_{fuel} = 0.1111\,\mathrm{g/s}$) yielding a global equivalence ratio of $\phi_{glob} = 0.89$. Flow variations in the experiment may cause a variation of the resulting laminar flame speed, but since the latter changes by less than $\pm 1\%$ of its nominal value, variations are not considered in the simulation, nor are they observed experimentally. All inlet temperatures are set to $T = 300\,\mathrm{K}$. A pressure boundary condition is imposed at the atmosphere outlet (1 bar). As discussed in Sec. 3.4, the near-wall flow is modeled in the entire combustion chamber and injector. Wall temperatures are set to $T_w = 300\,\mathrm{K}$ in this study. A characteristic quartz response time can be computed as $\tau_{cond} = \delta^2 \rho C/\lambda = 30.68\,\mathrm{s}$ (for a thickness of $\delta = 5\,\mathrm{mm}$) and is three orders of magnitude larger than the light-round times discussed later. The thermal conductivity λ, density ρ and specific heat C are specified by the quartz manufacturer [70]. We can thus impose a constant wall temperature and ignore heating of the walls.

Liquid phase boundary conditions are set to allow elastic rebound in the combustion chamber. In the injectors, droplet–wall interactions are considered to be predominant, thus requiring a film-type boundary condition as developed in [71].

3.6. Initial conditions and ignition procedure

Initial conditions are deliberately chosen to ensure a successful ignition and the initial flame kernel to survive the first stages of its development.

It is emphasized once more that these early stages are beyond the scope of this work. Instead, as mentioned in the introduction, we focus specifically on the light-round phase [1, 2]. The combustion chamber is prefilled with a fuel/air mixture in the experiment for a few seconds before sparking. Since n-heptane is a volatile fuel, evaporation already occurs under ambient conditions. Stationary equivalence ratios are attained after around one second, but vary with chamber height due to a complex heterogeneous flow structure.

In an attempt to match these initial conditions of the experiment as best as possible, the simulation first starts with fuel injection and no combustion. Taking advantage of the rotational symmetry of the combustor, pre-fueling is performed on one eighth of the full geometry including the atmosphere, greatly reducing computational costs. During this specific phase, periodic boundary conditions are applied to the tangential faces of the domain. The equivalence ratio is monitored over time until steady average values can be observed on several cut-planes at different heights. Second, the converged solution is cloned eight times (including the geometry) to yield the full annular combustor assembly. Third, the fuel injection phase is resumed in the actual full annular geometry for 24 ms to dissolve coherent flow structures resulting from the cloning procedure. The required simulation time of this step is derived from the autocorrelation rate of velocity fluctuations which is estimated as $\tau_{corr} = 6\,\mathrm{ms}$. Lastly, a $10 \times 24\,\mathrm{mm}$ ellipse of burnt gases is introduced at the experimental spark plug position to act as an initial flame kernel and ensure a successful and robust ignition procedure.

4. Results

Before we derive a simplified model for flame propagation during light-round with cold combustor walls, we first draw the attention to the propagation mechanism under these conditions. The effects of liquid fuels and heat losses are studied both from a global perspective as well as locally on particular points on each propagating flame front. The role of the dynamic combustion model is also briefly outlined.

4.1. Flame propagation during light-round

To approach the simulation results from a global perspective, it is useful to examine instantaneous snapshots of different stages during light-round shown in Figure 6. Unless explicitly stated otherwise, the instant the simulation starts is used as time reference $t_0 = 0\,\mathrm{ms}$ (flame kernel delivered in the outer recirculation zone of the first burner). The images are obtained by transforming the full cylindrical chamber into a rectangular system and integrating the heat release rate in line-of-sight direction. In these transformed images, the flames propagate from the center (position of the initial flame kernel shown in Fig. 6(a)) to the sides. The nozzle outlets of the sixteen injectors are included at the bottom of each image for reference.

All characteristic phases of light-round and their corresponding flame shapes are well retrieved in the simulation and are consistent with the experimental high-speed imaging performed by Prieur et al. [21]. Identical flame shapes are also observed in Refs. [28, 34] which provide detailed analyses for the interested reader.

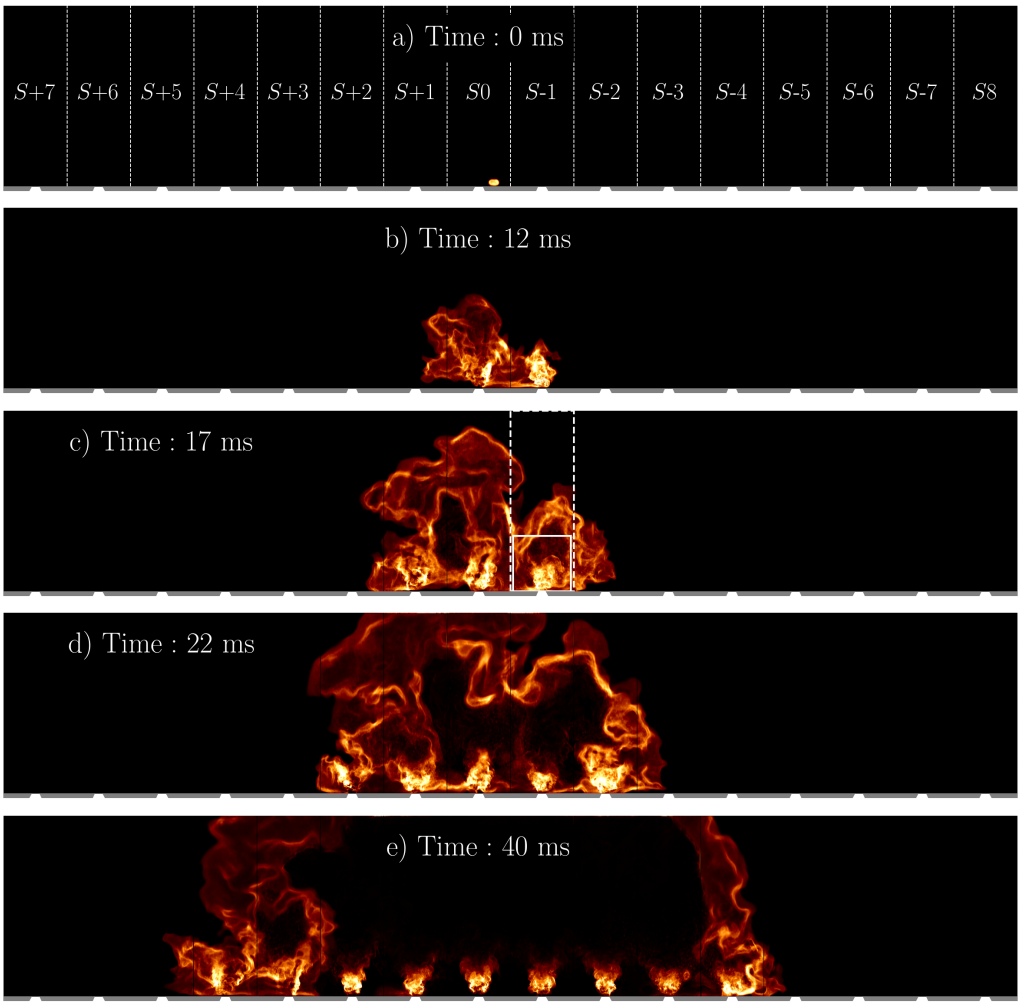

Figure 6: Line of sight integration of heat release rate in LES for different instants after transforming the chamber from a cylindrical into a rectangular system. Sectors are labeled according to Fig. 1(c). Image c) (here) illustrates the sector volume considered for heat release rate integration as discussed in Sec. 4.2: solid line: chamber clipped at a height of 60 mm; dashed line: full chamber height.

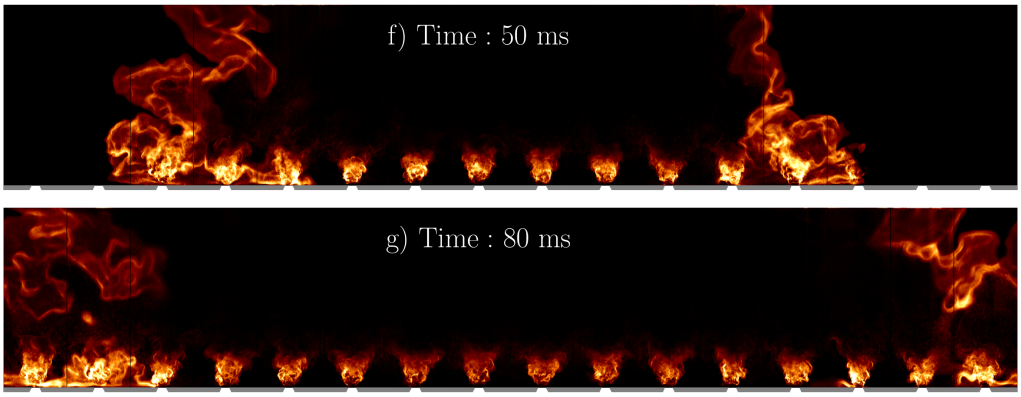

Figure 6: Line of sight integration of heat release rate in LES for different instants after transforming the chamber from a cylindrical into a rectangular system (cont.).

4.2. Light-round duration

To compare the simulation with experimental data, the light-round duration is commonly used as a global metric, defined here as the elapsed time between two specific events during ignition. Synchronization between LES and experiment is usually established once the initial flame (starting from the sector $S0$ marked with a bolt in Fig. 1(c)) has ignited the *adjacent* burner in sector S-1 (marked with a star in Fig. 1(c)). This common starting point eliminates at least those uncertainties associated with the stochastic behavior of the initial spark and the subsequent growth of the initial flame kernel. Hence the focus on phase IV of light-round [1, 2].

Conversely, the end of light-round can be determined more easily by taking the first recorded frame obtained from high-speed imaging (instantaneous solution in the case of LES) in which the two flame fronts start to overlap. The time difference between this instant and the synchronization point defined above yields the light-round duration τ^{LR}.

Case	τ^{LR} [ms]	Case	τ^{LR} [ms]
EXP1	51.2	BASE	54.6
EXP2	52.7	ADIAB	43
EXP3	52.4		
EXP4	43.4		

Table 1: Light-round durations of four experimental runs [24] with combustor walls at ambient temperature ($T_w = 300\,\mathrm{K}$). The simulated light-round duration is given for the baseline case (BASE) for the same conditions as in the experiment. An additional simulation with adiabatic combustor walls (ADIAB) is also carried out for comparison. Numerical light-round durations are computed as visualized in Fig. 7.

Following this definition, light-round durations for four experimental runs (EXP1 - EXP4) [24] and one simulation with cold combustor walls (referred to as baseline case, abbreviated as BASE) are compiled in Tab. 1. A complementary simulation (ADIAB) carried out using adiabatic wall boundary conditions only, is already listed here, but discussed later. Despite the lack of an unambiguous definition of τ^{LR}, the predicted duration (baseline case) agrees fairly well with the experimental data. Note that case EXP4 qualifies as an outlier, since experimental conditions were less well controlled for this specific run. Data obtained from other configurations and at different operating points suggests that there is only a very moderate variability of the experimental light-round duration between subsequent runs. We expect this to hold true for the present configuration as well and keep the entry EXP4 for the sake of completeness.

The inherent ambiguity for all definitions of a synchronization point between experiment and simulation clearly deserves further discussion. A metric (*i.e.* "sensitivity") for the assessment of the numerical light-round duration is worth defining, rather than considering it as an exact measure. Reasonable definitions (numbered (i) to (iii)) can be based for example on a specific value of the heat release rate or the instant the propagating flame front in the negative chamber half H- has crossed a certain sector. In the former case, the heat release rate in sector S-1 is volume integrated and the instant of its peak value is used as synchronization point. The solid lines in Fig. 7 show the per-sector heat release rate for sectors S-1 to S-8 when performing the volume integral up to a height of 60 mm. Thus, the light-round duration (i) $\tau^{LR} = 54.6\,\mathrm{ms}$ corresponds to the time difference between the two vertical dash-dotted lines in Fig. 7, *i.e.* the heat release peak in sector S-1 and the instant the propagating flame fronts start to overlap. Limiting the volume integration up to 60 mm aims at focussing on the attached flame at the burner while excluding heat release contributions from above and neighboring sectors (cf. solid line box in Fig. 6(c)). Performing the volume integral over the full chamber height instead results in a delayed peak in sector S-1 as visualized by the dashed line in Fig. 7, yielding a value of (ii) $\tau^{LR} = 52.6\,\mathrm{ms}$ (cf. dashed box in Fig. 6(c)). The peak shift between the dashed line and the thick solid line (in Fig. 7) may be interpreted as a sensitivity in terms of the employed definition (gray shaded area) and is less than 4% of the overall light-round duration τ^{LR}.

A third possible definition of the light-round duration can be derived from the instant at which the circumferentially outermost flame edge has entirely

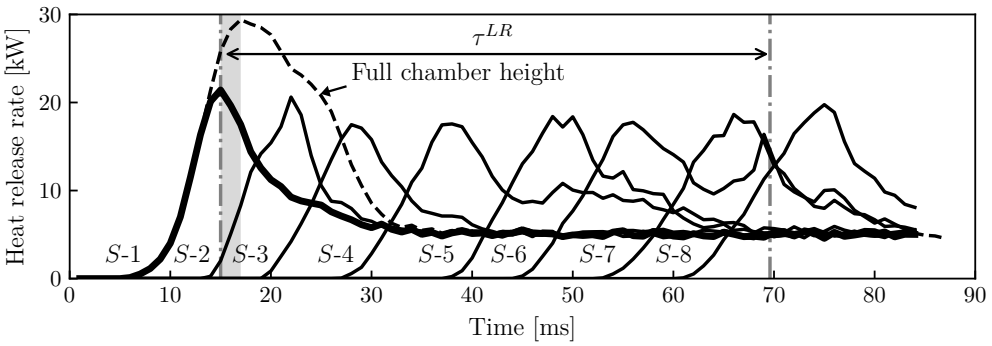

Figure 7: Volume integrated heat release rate (gray shaded area) per sector in the negative half without clipping (dashed line, first sector only) and clipped to a height of 60 mm (solid lines). The light-round duration τ^{LR} corresponds to the difference between the peak heat release in sector S-1 and flame front merging (vertical dash-dotted lines). The sensitivity associated with the definition of the synchronization point corresponds to the peak shift between the thick solid and the dashed line.

crossed sector S-1: (iii) $\tau^{LR} = 49\,\text{ms}$, equivalent to sensitivity of 10% at worst, when using definition (i) as reference.

In summary, the light-round duration is deemed to be only moderately impacted by the choice of the definition for the synchronization point, yielding very acceptable results in either case, compared to the duration reported in experiments. The modeling setup then allows to describe the flame propagation quantitatively in the considered configuration that is characterized by cold walls. We reiterate that our critical assessment is meant to highlight a sensitivity with regard to the employed definition (due to the lack of a straightforward metric) and we do *not* intend to simply choose the definition which best fits our numerical results.

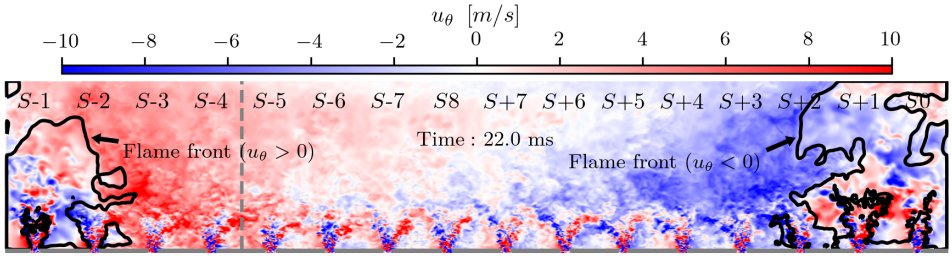

Figure 8: Azimuthal velocity u_θ on an unwrapped cylindrical cut-plane at $R = 0.175\,\mathrm{m}$. Dark shades correspond to high azimuthal velocities (from left to right and vice versa). Solid contour lines of iso-values of the progress variable ($c = 0.76$) indicate the instantaneous flame position. Axial velocity profiles are plotted along the dashed vertical line in Fig. 9.

4.3. Volumetric expansion of burnt gases

The most important driving mechanism of flame propagation consists in a flow acceleration in azimuthal direction during the volumetric expansion of burnt gases inside the chamber as illustrated in Fig. 8. Examining the azimuthal velocity u_θ on this unwrapped cylindrical cut-plane at $R = 0.175\,\mathrm{m}$ reveals dark shades upstream of each flame front representing high flow velocity values (red: from left to right, blue: vice versa). Lighter shades in turn indicate close to zero azimuthal velocity. The instantaneous flame position is visualized by black contour lines of the progress variable at $c = 0.76$ (peak of fuel species source term). The selected value is an arbitrary choice and used for visualization purposes in our figures. Results are insensitive to the chosen value. The sector layout in Fig. 8 still refers to the nomenclature of Fig. 1(c) and applies henceforth to all following unwrapped cutplanes.

It is worth noting that the effect of the volumetric burnt gas expansion can be observed several sectors ahead of each flame front, although not uniformly

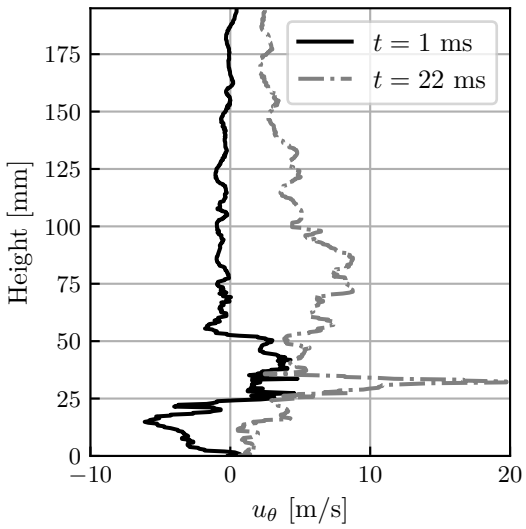

Figure 9: Axial velocity profile of the azimuthal velocity u_θ sampled along the dashed line in Fig. 8.

over the chamber height. Two instantaneous azimuthal velocity profiles are sampled along the dashed sampling line in Fig. 8 and plotted in Fig. 9. Initially ($t = 1\,\mathrm{ms}$), no mean azimuthal flow is observed except for the flow perturbations induced by the swirlers between the chamber bottom and up to 50 mm above (solid line in Fig. 9). The velocity profile exhibits at a later time $t = 22\,\mathrm{ms}$ positive values across the entire chamber height (dash-dotted line in Fig. 9), which is an indication of the flow acceleration induced by burnt gas expansion. It is most pronounced at 30 mm above the chamber bottom, where it reaches $u_\theta = 20\,\mathrm{m/s}$, around four times of its initial value at the same height. This strong velocity peak raises the question how fuel droplets react to this effect and interact with the flame on a local scale.

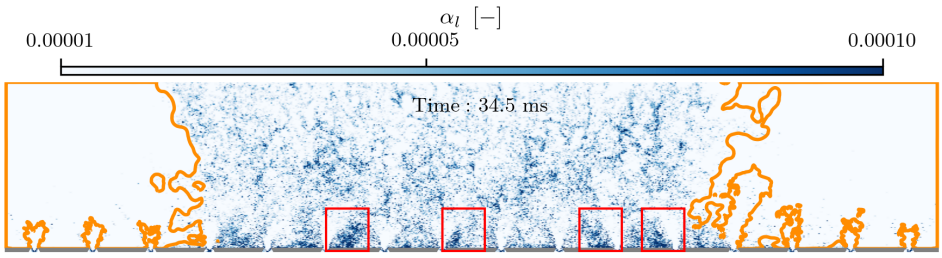

Figure 10: Liquid volume fraction α_l on an unwrapped cylindrical cut-plane at $R = 0.175\,\mathrm{m}$. Orange contour lines correspond to iso-values of the progress variable of $c = 0.76$. Droplet accumulations in the wake of the swirling jets are highlighted by red squares. Sector layout as in Fig. 8.

4.4. Flame interaction with droplets

In Fig. 10, the flame/droplet interaction induced by the flow acceleration through burnt gas expansion is visualized on the same unwrapped cylindrical cut-plane at $R = 0.175\,\mathrm{m}$ as before, with orange contour lines representing the progress variable ($c = 0.76$). A representative time frame at $t = 34.5\,\mathrm{ms}$ (propagation as two separate flame fronts) is chosen for an optimal visibility of the phenomenon on that plane. Dark shaded regions indicate an increased liquid volume fraction α_l and can be interpreted as droplet accumulations. Crucially, these accumulations prevail mostly in the wake of the swirling jets close to the chamber bottom (see squares in Fig. 10). Droplets entering the combustion chamber ahead of the propagating flame fronts deviate from their initial upward trajectory due to the burnt gas expansion and are trapped in the recirculating flow between adjacent injectors, similar to jet in crossflow configurations [30]. As a consequence, the flame may locally burn in richer conditions than the overall global equivalence ratio, once it encounters such a droplet accumulation. These accumulations appear (more clearly than

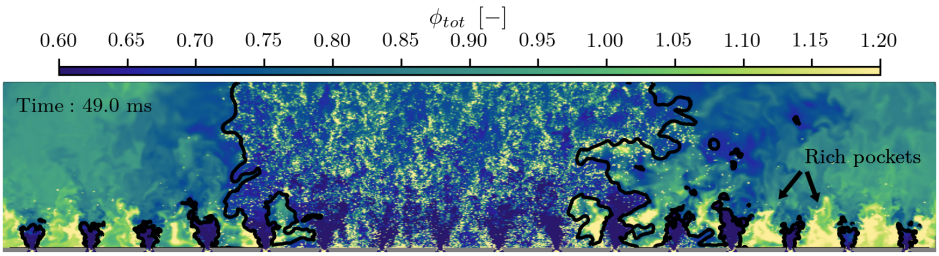

Figure 11: Total equivalence ratio ϕ_{tot} on an unwrapped cylindrical cut-plane at $R = 0.175\,\mathrm{m}$. Contour lines correspond to iso-values of the progress variable of $c = 0.76$.

Fig. 10 may suggest) in Fig. 11 as rich pockets of increased equivalence ratio (light shades), specifically in the burnt gases, proving that droplets *remain* trapped in the recirculation zones between adjacent burners. The amount of accumulated droplets is certainly subject to temporal variations of the flame expansion in the combustion chamber. Note that the total equivalence ratio ϕ_{tot}, the sum of the gaseous and liquid equivalence ratio, plotted in Fig. 11 is essentially identical to the gaseous equivalence ratio in the burnt gas region, where contributions from liquid fuel is barely present. By contrast, the total equivalence ratio is more heterogeneous in the fresh gas region due to a spatially varying contribution from droplets.

The leading point (LP), *i.e.* the circumferentially outermost flame edge in each half of the combustor, appears to avoid regions with high droplet accumulations in favor of regions with a lower overall liquid volume fraction. The leading point trajectory tracked in Fig. 12 thus exhibits a characteristic sawtooth form as it is more favorable to pass *over* droplet accumulations instead of right through them. This leading point behavior is attributed to the fact that propagation along regions of lower liquid volume fraction is faster as it requires fewer droplets to evaporate. We also note that the local

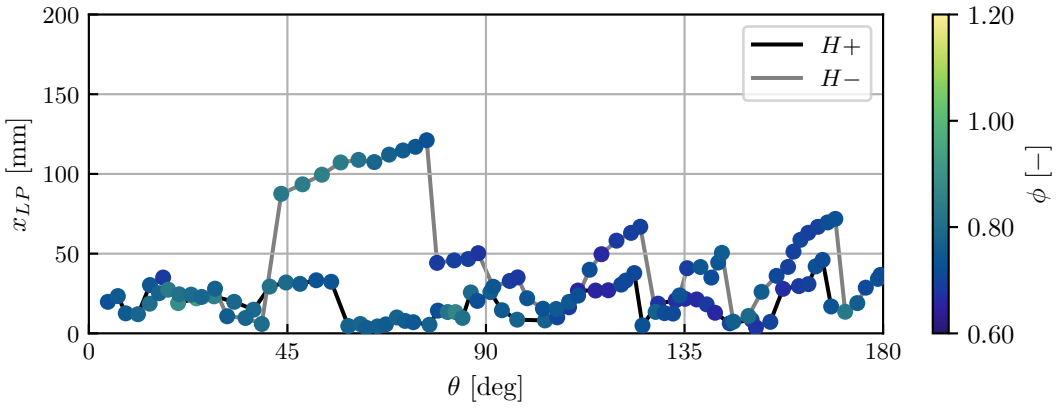

Figure 12: Leading point trajectory in each half of the chamber. Abscissa is given as arc length in degrees counting from sector S0 (see Fig. 1(c)). The ordinate corresponds to the leading point height above the chamber bottom. Colored markers indicate the local equivalence ratio ϕ.

equivalence ratio at the leading point (colored markers in Fig. 12) is lower than the global equivalence ratio $\phi_{glob} = 0.89$.

These findings support our stance (in particular the first goal mentioned in Sec. 1) to employ a polydisperse description of the liquid phase and a carefully adjusted injection model. The spray heterogeneity and flame/droplet interactions critically affect the flame trajectory and thus the light-round duration in the present configuration. The sawtooth-like leading point behavior in particular is even more striking when compared to previous works on flame propagation in multi-burner configurations: in [6], an increased burner-to-burner spacing enforces a sawtooth propagation pattern along connecting "bridges" of neighboring spray branches, since the inter-injector region close to the combustor backplane is too lean to be ignitable. Insufficient fuel/air mixing due to high equivalence ratios and low bulk-flow velocities constitute

another reason for sawtooth propagation [11]. By contrast, the flame itself causes its characteristic sawtooth trajectory in the present work by generating upstream droplet accumulations during burnt gas expansion, and these accumulations are less favorable to cross.

4.5. Impact of wall heat losses

Combustor wall temperatures not only affect the propagation pattern though. With the *a priori* study by Puggelli et al. [24] in mind, a comprehensive *a posteriori* analysis of the effect of wall heat losses on flame propagation can now be provided in the present work. In particular, the relation between heat losses and burnt gas expansion is brought to the reader's attention. Differences are pointed out with regard to the complementary ignition simulation (ADIAB) which is based on the exact same setup except for the wall boundary condition set to be adiabatic instead. This second ignition case also starts from the very same initial solution as its isothermal counterpart.

We recall that the adiabatic case is included to pursue our goal to quantify heat losses from an *a posteriori* perspective. Most importantly, the altered thermal boundary condition preserves the (upstream) equivalence ratio field upon which the laminar flame speed chiefly depends. Differences observed in case ADIAB can therefore be related more clearly to the effect of heat losses.

4.5.1. Heat release rate and wall heat fluxes

Similar to previous works, the heat release rates (HRR) follow a characteristic evolution during each stage of light-round (Fig. 13). Each curve is obtained by integrating the local heat release rate over the combustor vol-

ume without the surrounding atmosphere. While the slope is initially more moderate, a steep increase of the heat release rate is observed up to almost twice the nominal thermal power ($\mathcal{P}_{th}$) of the combustor. Once the flame-arch reaches the outlet of the chamber, heat release rates slightly decrease before increasing again, and reach roughly 2.5 times of $\mathcal{P}_{th}$ at the instant both flame fronts start to merge (diamond marker in Fig. 13). Residual parts of the flame fronts leave the chamber during transition into steady-state operation, causing a steep decrease of the heat release rates until $\mathcal{P}_{th}$ will eventually be reached. Both cases were stopped prior to steady-state operation due to constraints in available computational hours. Nevertheless, it can be inferred from Fig. 7 that each burner operates at approximately 5 kW after full ignition (already visible for burners in sectors S-1 to S-7), which totals in $\mathcal{P}_{th}$ for all 16 burners.

For an overall quantification of the wall heat losses $\dot{Q}$, all heat fluxes (both lateral walls and chamber bottom) are summed up and related to the nominal thermal power output $\mathcal{P}_{th}$ of the combustor (when fully ignited) in Fig. 13. Note that these fluxes from the fluid onto the combustor walls are deliberately chosen to have a positive sign.

The sum of all wall heat fluxes across the chamber walls exhibits a steady increase up to 50% of $\mathcal{P}_{th}$ (grey line in Fig. 13) towards the end of light-round. Viewed from the perspective of the simulation case ADIAB where all walls are adiabatic, heat losses account for a 27% longer light-round duration ($\tau^{LR}_{\mathrm{ADIAB}} = 43\,\mathrm{ms}$ versus $\tau^{LR}_{\mathrm{BASE}} = 54.6\,\mathrm{ms}$).

To understand how heat losses act on the driving mechanism of flame propagation, local effects have to be taken into account; these effects are

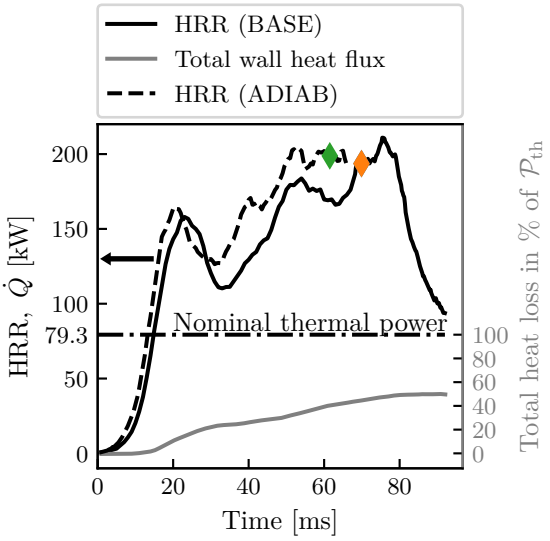

Figure 13: Evolution of the volume-integrated heat release rate (HRR) for the baseline case (solid line) and adiabatic case (dashed line). In the baseline case, total wall heat fluxes $\dot{Q}$ are plotted as gray line in absolute values (left axis) and in percent of the nominal thermal power $\mathcal{P}_{th}$ of combustor (right axis). Diamonds mark the instant at which the propagating flame fronts start to merge in each case.

investigated in the following subsection.

4.5.2. Index of heat loss

The heat loss index I_{HL} may be considered as a useful metric to visually inspect the cooling of burnt gases (for case BASE), defined as:

$$I_{\mathrm{HL}} = \frac{h - h_{low}}{h_{adiab} - h_{low}} = \begin{cases} 1 & \text{adiabatic} \\ 0 & \text{max. local heat loss} \end{cases} \tag{9}$$

where h denotes the local enthalpy, h_{low} the enthalpy of the local mixture, if it had the temperature of the combustor walls (*i.e.* ambient temperature), and h_{adiab} the enthalpy of the local mixture in perfect adiabatic conditions. Since the values of h_{adiab} (adiabatic mixture) and h_{low} (mixture at ambient temperature) are chosen deliberately, I_{HL} reaches unity, if the local mixture is equivalent to an adiabatic mixture, and lower values, if it incurs heat losses.

Upon examination of the unwrapped cutplane at $R = 0.175\,\mathrm{m}$, different regions with different levels of heat losses can be identified: burnt gases far downstream from each flame front (labeled as (1) in Fig. 14) take values of $I_{\mathrm{HL}} < 0.7$ as they have been exposed longer to the combustor walls than burnt gases immediately downstream of the flame fronts (labeled as (2)). In fact, large parts of the flame fronts propagate in almost adiabatic conditions ($I_{\mathrm{HL}} \approx 1$) across the full chamber height (on the presented cut-plane). Therefore, the longer the (downstream) burnt gases are in contact with the combustor walls, the more pronounced the heat loss effects, particularly towards the end of light-round. In turn, the fresh gas region labeled as (3) in Fig. 14 remains adiabatic, since fluid and walls are both at ambient temperature. The effect of evaporative cooling (particularly in the fresh gases) is

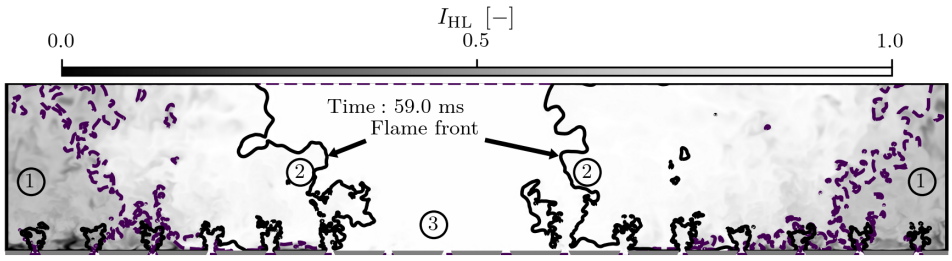

Figure 14: Heat loss index I_{HL} on an unwrapped cylindrical cut-plane at $R = 0.175\,\mathrm{m}$. Unity values mark fully adiabatic zones, zero marks the highest local heat loss possible. Solid contour lines correspond to iso-values of the progress variable of $c = 0.76$. Dashed contours limit zones where $I_{\mathrm{HL}} \leq 0.7$.

comparably small and barely alters the fresh gas enthalpy.

As already discussed in [4], the flow acceleration during burnt gas expansion, and thus the flame propagation speed, is proportional to the density ratio between fresh and burnt gases. Crucially, this density ratio may be altered due to heat transfer between hot burnt gases and combustor walls at ambient temperature. Volume-averaging the density in the burnt gas volume inside the chamber (denoted by angular brackets with subscripted "V") reveals a clear trend: since density and temperature are inversely proportional, the burnt gas density steadily increases with decreasing burnt gas temperature. In Fig. 15, this relation is conveniently plotted as density ratio $\langle \rho_u \rangle_V \,/\, \langle \rho_b \rangle_V$ to highlight the decaying driving effect of flame propagation (solid line). In turn, the density ratio in the adiabatic case (dashed line in Fig. 15) remains almost constant during the propagation of two separate flame fronts. A moderate decrease is observed at the end of this case when fresh air from the environment is entrained at the combustor outlet.

Therefore, an appropriate wall model in the baseline case is deemed es-

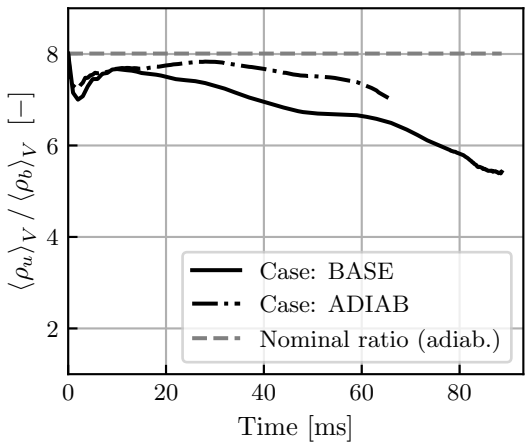

Figure 15: Density ratio (proportional to the volumetric burnt gas expansion) for the baseline case (solid line) and ADIAB (dash-dotted line). For reference, the nominal density ratio of adiabatic burnt gases at the global equivalence ratio $\phi_{glob} = 0.89$ and fresh gases is added as dashed line.

sential to correctly predict wall heat transfers and thus the light-round duration under such conditions. A comparison with a classical logarithmic wall model similar to Ref. [24] can be found in Appendix B. The intricate relation between heat losses, the density ratio and the turbulent flame propagation speed is further discussed in Sec. 5 based on a mathematical model.

4.6. Flame/turbulence interactions

In light of the recent study published in Ref. [34], the interaction of the flame with turbulence deserves further attention as well. This aspect is considered to be particularly relevant for the present case, since the flame surface wrinkling parameter β cannot be assumed constant over the entire flame. For a highly transient and inhomogeneous case such as light-round ignition, little physical argument can be made for a "universal" (*i.e.* constant) β. Therefore,

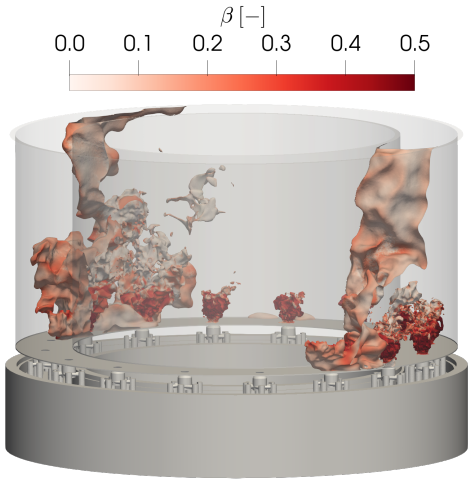

Figure 16: Flame surface wrinkling parameter β.

it is more appropriate to employ a dynamic combustion model for light-round simulations, independently from the thermal boundary conditions (see also [34]).

On a representative iso-surface of the progress variable $c = 0.76$ for a given instant $t = 44\,\mathrm{ms}$ (Fig. 16), both propagating flame fronts exhibit a comparably low wrinkling parameter ($\beta \approx 0.18$), while the stabilized flames downstream show higher values instead ($\beta \gtrsim 0.4$). Note that the color map is deliberately clipped to help distinguish β values on the flame fronts from ignited flames downstream.

The corresponding distribution of β on the flame surface is given for the same instant in Fig. 17 (solid line). The bin colors match the shading of the iso-surface in Fig. 16. Two major conclusions can be drawn from the PDF: first, the distribution of values of the wrinkling parameter is non-uniform. While the peak in the PDF at $\beta \approx 0.18$ originates from the propagating

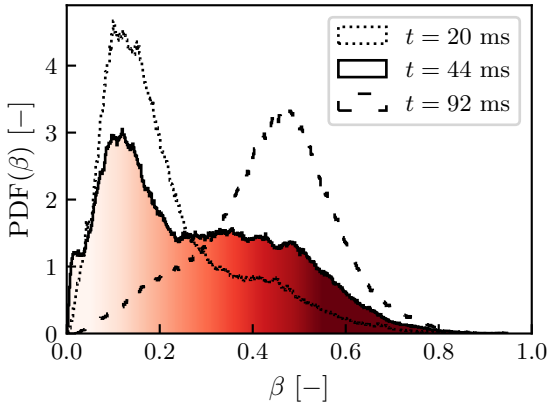

Figure 17: Distribution of flame surface wrinkling parameter β.

flame fronts, the ignited and stabilized flames take a wider range of values of $\beta \gtrsim 0.4$.

Second, the PDF considerably changes its shape over time. During the early stages of light-round, *i.e.* when the flame develops an arch-like form, only few burners are already ignited so that the peak in the PDF at $\beta \approx 0.18$ (cf. Fig. 17, dotted line) is initially more pronounced. The plateau at $\beta \gtrsim 0.4$ in turn is much less developed. However, the more burners are ignited during flame propagation, the more the plateau develops while the peak associated with the propagating flame fronts gradually diminishes. Once the entire combustor is fully ignited and reaches a steady state, the PDF transitions into a single-peak PDF at $\beta = 0.47$, since there is no contribution from the propagating flame fronts any more (dashed line in Fig. 17). This evolution of the wrinkling parameter β is consistent with the analysis in [34] and occurs independently of the wall boundary conditions.

5. Analysis

The previous section provides insights into the governing mechanisms of flame propagation during light-round without quantifying their individual impact on the propagation speed yet. Therefore, a macroscopic flame speed model is derived here for the present configuration to put forward the argument that *all* phenomena previously discussed have to be taken into account in the simulation. First, the model is benchmarked in terms of its prediction capabilities using the data obtained from the baseline case. Second, the flame speed model is decomposed to identify the terms and variables which are affected by the main physical phenomena studied in this work. Third, *a priori* estimations for the flame propagation speed under *different* conditions are computed using the macroscopic model to underscore the fact that neither phenomenon can be neglected.

5.1. Model for the absolute flame propagation speed during light-round

Deriving an expression for the turbulent absolute flame speed S_a^T (also referred to as flame propagation speed) requires several macroscopic balance equations for the burnt gas mass. The equations are presented here in a condensed form, but the interested reader may find a complete step-by-step guide in Refs. [34, 72] for adiabatic conditions. At this point, it should be clarified that the final expression for the flame speed is only valid when the flame propagation mode can be described as two separate, semi-confined flame fronts, limited by the chamber backplane, the lateral combustor walls and the combustor outlet. During this stage in the ignition process and with the approximation of the separate flame fronts as vertical planes, the rate

change of the burnt gas volume V_b inside the combustion chamber is written as:

$$\frac{dV_b}{dt} = S_a^T A_0 \tag{10}$$

where the sectional surface area of the planes is $A_0 = 2h\Delta R$ (chamber height h and width ΔR computed as difference between outer and inner chamber radii). Next, the macroscopic balance equation of the progress variable within the combustor is given as:

$$\frac{dm_b}{dt} = \dot{m}_b^{in} - \dot{m}_b^{out} + \int_V \dot{\omega}_c dV \tag{11}$$

introducing the mass flow rates of burnt gases at the inlet (in case of any recirculation there) and outlet of the combustion chamber ($\dot{m}_b^{in}$ and $\dot{m}_b^{out}$), and the source term of the progress variable $\dot{\omega}_c$. The volume integral in Eq. 11 allows for introducing the LES flame consumption speed S_c^{Δ} through the following expression:

$$\langle \rho_u \rangle A_{res} S_c^{\Delta} = \int_V \dot{\omega}_c dV \tag{12}$$

where $\langle \rho_u \rangle$ denotes the averaged fresh gas density and A_{res} the resolved flame surface. In the context of LES, the consumption speed can be computed from the laminar flame speed S_l and the sub-grid scale flame surface wrinkling $\langle \Xi_{\Delta} \rangle_{res}$ averaged over the resolved flame surface

$$S_c^{\Delta} = \langle \Xi_{\Delta} \rangle_{res} S_l. \tag{13}$$

Eventually, the mass of burnt gases m_b can also be written as:

$$m_b = \langle \rho_b \rangle_V V_b \tag{14}$$

where $\langle \rho_b \rangle_V$ denotes the volume averaged burnt gas density. Differentiation of Eq. 14 with respect to time and substituting the corresponding terms with Eqs. 10 - 13 yields the final expression for the absolute turbulent flame speed:

$$S_a^T = \underbrace{\frac{\langle \rho_u \rangle_V}{\langle \rho_b \rangle_V} \Xi_{res} \langle \Xi_\Delta \rangle_{res} S_l}_{\text{Term I}} - \underbrace{\frac{\dot{m}_b^{out} - \dot{m}_b^{in}}{\langle \rho_b \rangle_V A_0}}_{\text{Term II}} - \underbrace{\left(\frac{V_b}{\langle \rho_b \rangle_V A_0} \frac{d\rho_b}{dt} \right)}_{\text{Term III}}. \quad (15)$$

The resolved flame surface wrinkling, $\Xi_{res} = A_{res}/A_0$, is defined as ratio between the resolved flame surface and the sectional surface area A_0 of the combustor.

Figure 18 shows the temporal evolution of S_a^T computed according to Eq. 15 for the baseline case (top) and case ADIAB (bottom) as thick solid lines. The masked time span at the beginning (in gray) indicates that Eq. 15 cannot be applied during the first phase of light-round by construction, as the initial flame has not yet developed two separately propagating flame fronts. Averaging S_a^T over the valid time span up to flame front merging yields 8.81 m/s for the baseline case and 10.03 m/s for the adiabatic case.

A meaningful reference velocity may be computed from one sector arc length (*i.e.* $s = 2\pi R/16$) and the averaged time between two consecutive sector heat release peaks (obtained from Fig. 7) in order to assess the accuracy of the modeled flame propagation speed S_a^T. These propagation speeds are subscripted with "HR" in the following. For the baseline case, a velocity of $\mathcal{S}_{a,\mathrm{HR}}^T = 7.6\,\mathrm{m/s}$ is obtained. This reference velocity is plotted as horizontal gray dashed line in Fig. 18 (for the flame branch in H-, see Fig. 1(c)) and is fairly well retrieved by the modeled velocity suggesting that the major physical phenomena involved in flame propagation during light-round are accurately captured. The same holds true for case ADIAB, which yields

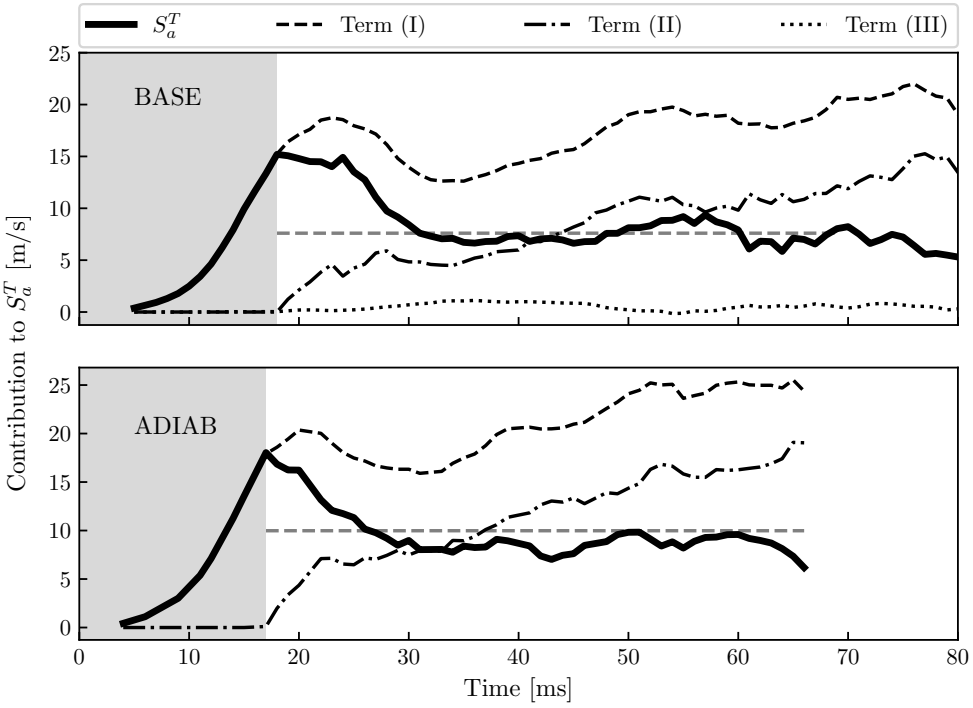

Figure 18: Decomposition of Eq. 15 into three main terms (thin lines) plotted as absolute values for both cases. The absolute turbulent flame speed S_a^T (thick line) is added for reference. The horizontal dashed grey lines correspond to the average velocity obtained from the sector arc length and the averaged elapsed time between two adjacent sector heat release peaks of the respective case (see Fig. 7 for the baseline case).

$\mathcal{S}^T_{a,\,\mathrm{HR}} = 9.98\,\mathrm{m/s}$.

Equation 15 may be split into its three main parts (indicated by curly braces) to identify the leading terms. It is recalled that Term I resembles the classical expression for a turbulent spherically propagating flame or a developing flame in a closed duct, Term II arises due to the fact that the control volume (*i.e.* the combustion chamber) is semi-confined and Term III appears as a consequence of temporal density variations. Each of these terms is plotted in absolute values in Fig. 18 (black dashed lines) and reveals an interesting result. Essentially, Eq. 15 is governed by Terms I and II, while the effect of temporal density variations (Term III) appears to be almost negligible. The evolution of Term II is directly linked to $\dot{m}_b^{out}$: it is zero until the initial flame arch has reached the chamber outlet. At that point, the outflux of burnt gases starts to increase (as does Term II) with the propagation of the flame fronts. Furthermore, comparing the baseline case to ADIAB shows that in the absence of wall heat losses Terms I and II are shifted to higher velocities. This suggests that the main physical phenomena described in Sec. 4 are interdependent, *i.e.* react and adapt to deliberately introduced changes in the operating or boundary conditions, as is the case with deactivating wall heat transfers in Large-Eddy Simulations. These phenomena are therefore studied in detail in the following section.

5.2. Model decomposition

Apart from splitting Eq. 15 into its main terms, more insights into the main mechanisms of flame propagation can be gained when examining the governing physical phenomena individually and establishing links to the relevant variables in the model equation.

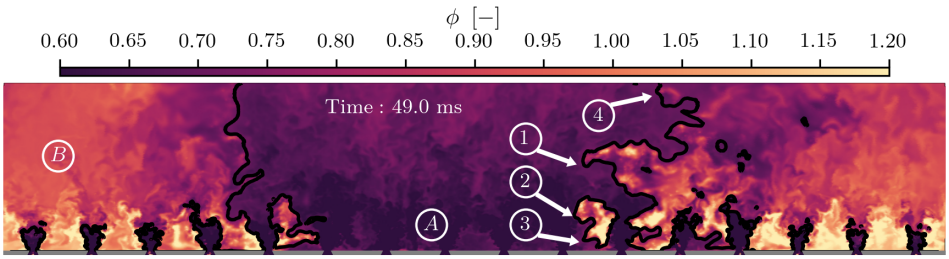

Figure 19: Gaseous equivalence ratio ϕ on an unwrapped cylindrical cut-plane at $R = 0.175\,\mathrm{m}$. The one-dimensional consumption speed S_c^{1D} is computed for Fig. 21 at the four labeled positions at the flame front. Contour lines correspond to iso-values of the progress variable of $c = 0.76$.

5.2.1. Laminar burning velocity and two-phase flow

The effects of the liquid phase on the absolute turbulent flame speed S_a^T enter through the laminar flame speed S_l appearing in Term I of Eq. 15 and are twofold. First, the equivalence ratio field ϕ is strongly heterogeneous due to complex interactions of droplets with the flow and different amounts of liquid and pre-vaporized fuel along the propagating flame fronts. For example, ϕ ranges from roughly $\phi = 0.7$ in the fresh gases (labeled as A in Fig. 19) up to $\phi = 0.95$ in the burnt gases in the upper half of the combustion chamber where all droplets are fully evaporated (labeled as B). In rich recirculation zones between adjacent burners, ϕ is larger than unity as a consequence of droplet accumulations. The mixture inhomogeneity then presumably prevents the identification of S_l with the theoretical laminar flame speed $S_l^0(\phi_{glob})$ determined trivially from the global equivalence ratio, at which the combustor is operated.

Second, the gaseous equivalence ratio ϕ can also be seen to increase across the flame fronts in Fig. 19, underscoring the intrinsic two-phase flow structure

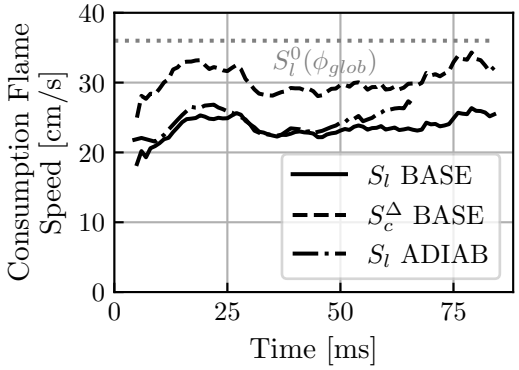

Figure 20: Flame consumption speeds averaged over the total flame front surface (S_l) for case BASE (solid line) and ADIAB (dash-dotted line). The dotted grey line corresponds to the theoretical laminar flame speed at global equivalence ratio $S_l^0(\phi_{glob})$. The consumption speed averaged over the resolved flame surface is given as dashed line for case BASE.

of the flame front within which droplets are evaporating. This two-phase structure of the flame surely impacts the resulting laminar flame speed S_l.

Therefore, it is more appropriate from a global viewpoint to consider an averaged laminar flame speed over the total flame surface $A_{tot} = \langle \Xi_\Delta \rangle_{res} A_{res}$, computed as:

$$S_l = \frac{1}{\rho_u A_{tot} Y_c^{eq}} \int_V \widetilde{\dot{\omega}}_{Y_c} dV \tag{16}$$

where the integral is performed over the combustor volume V and normalized by the equilibrium value of the progress variable species Y_c^{eq}. The resolved flame surface A_{res} is given as $A_{res} = \int_V |\nabla \tilde{c}| dV$ [73] which is also integrated over the combustor volume V, thus including the propagating flame fronts as well as the attached flames.

Plotting S_l according to Eq. 16 (or even according to Eq. 13 for S_c^Δ)

yields $S_l \approx 24\,\mathrm{cm/s}$ (or $S_c^{\Delta} \approx 30\,\mathrm{cm/s}$), while the theoretical flame speed at global equivalence ratio is $S_l^0(\phi_{glob}) = 36\,\mathrm{cm/s}$ (see Fig. 20). It also reveals similar laminar flame speeds of case BASE and ADIAB. This confirms that the changed wall boundary condition preserves the (upstream) equivalence ratio as intended upon which S_l primarily depends.

Figure 20 shows that the actual laminar flame speed is, on average, much lower than $S_l^0(\phi_{glob})$. This is attributed to the leaner conditions encountered by the flame during its propagation and to its two-phase flow nature. Indeed, it has already been established in the literature [18, 19, 74] that the laminar flame speed of two-phase flames obeys the relation $S_l \leq S_l^0$ in overall lean mixtures. This implies that the effective (or averaged) equivalence ratio which corresponds to the averaged laminar flame speed plotted above must be smaller than the global equivalence ratio as well.

To provide further evidence for this argument, an average equivalence ratio of $\phi_{S_l=24\,\mathrm{cm/s}} = 0.70$ can be obtained from the flame speed diagram in Fig. 21 assuming an average flame speed of $S_l = 24\,\mathrm{cm/s}$. This average equivalence ratio can then be compared to the probability density function of ϕ, PDF(ϕ), on a characteristic iso-surface of the progress variable $c = 0.76$, shown in Fig. 22. The distribution of the gaseous equivalence ratio on this iso-surface ranges from $\phi = 0.65$ to around $\phi = 1.2$ with a broader peak at $\phi = 0.7$ and matches the average equivalence ratio predicted by the flame speed diagram fairly well. As far as averaged quantities are concerned, the average (or effective) equivalence ratio for lean two-phase flames is proven to be lower than the overall equivalence ratio, leading to a lower laminar flame speed.

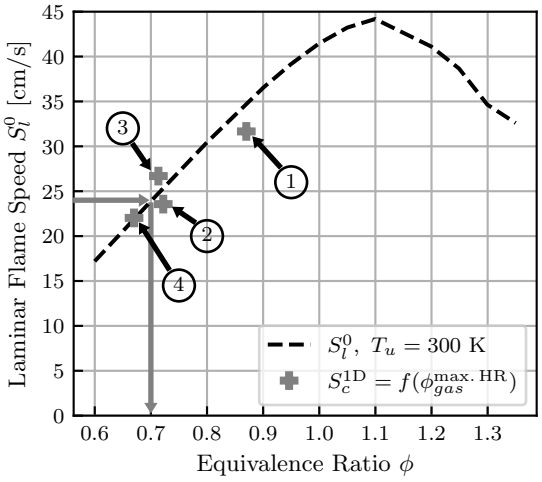

Figure 21: Laminar flame speed diagram for a gaseous n-heptane/air flame at varying equivalence ratios for $T_u = 300\,\text{K}$ in fresh gases. Dashed line denotes reference data published in [55]. Crosses refer to the one-dimensional laminar consumption speed S_c^{Δ} according to Eq. 17, which is computed for arbitrary locations along the flame front indicated in Fig. 19.

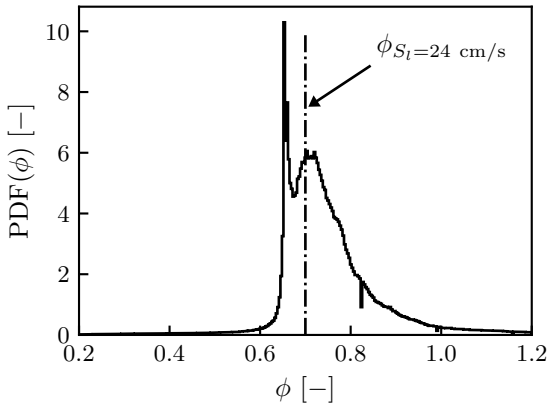

Figure 22: Histogram of gaseous equivalence ratio ϕ on a characteristic iso-surface of the progress variable $c = 0.76$.

This does certainly not preclude the existence of *local* variations of the flame speed along the propagating flame fronts. In fact, it can be shown that the local laminar flame speed of a two-phase flame relates to an effective equivalence ratio at peak heat release rate [19]. These values scatter around the average laminar flame speed of $S_l = 24\,\mathrm{cm/s}$ in the present case. Assuming that each flame front element behaves like a one-dimensional flame and that the consumption speed $S_c^{1\mathrm{D}}$ of such flame is equivalent to its laminar flame speed allows to apply Eq. 17 in direction of the three-dimensional flame front normal for arbitrary positions along the propagating flame fronts.

$$S_c^{1\mathrm{D}} = \frac{1}{\rho_u Y_c^{eq}} \int \dot{\omega}_{Y_c} dc \tag{17}$$

These positions correspond to the labels 1 - 4 in Fig. 19 and are plotted in Fig. 21 accordingly.

Given the assumptions made for the computation of such local flame speeds, all data points align remarkably well with reference S_l^0 values, although the local total equivalence ratio (gaseous and liquid) can be quite different from the local gaseous condition. Furthermore, the laminar flame speed tends to increase with increasing height above the chamber backplane, since droplets are more likely to fully evaporate the farther they penetrate the combustion chamber (data points 1 to 3). Although closest to the chamber outlet, data point 4 exhibits the lowest equivalence ratio due to dilution effects resulting from entrained air of the surrounding atmosphere. Regardless of the position on the flame front, all laminar flame speeds are found to be inferior to the theoretical laminar flame speed at global equivalence ratio [19]. Compared to a light-round case with a fully premixed gaseous mixture, liquid fuel affects the laminar flame speed as well as the resulting absolute

turbulent flame speed through Eq. 15.

We emphasize that this observation holds true despite the two-step reaction mechanism's insensitivity to strain effects. On one hand, values for S_l are very close to the corresponding laminar unstrained flame speed for a given equivalence ratio as a consequence of the reduced mechanism with a unitary Lewis number. On the other hand, the flame fronts are found to be exposed to moderate strain rate values with alternating sign and a mean value close to zero, independently from the reaction mechanism. Thus, averaging S_l over A_{res} results in flame speeds which are also close to the laminar unstrained flame speed, since local and unsteady strain effects vanish in the averaging procedure. Under those conditions, a two-step reaction mechanism can be an acceptable choice, despite its limitations in predicting strained flame speeds. Detailed reaction mechanisms however can improve the predictions of Eq. 17.

5.2.2. Burnt gas density and heat losses

As foreshadowed in Sec. 4.5, wall heat losses act on the burnt gas density $\langle \rho_b \rangle_V$, which appears in all terms of Eq. 15. In particular, the burnt gas expansion is affected as it scales with the density ratio $\langle \rho_u \rangle_V \,/\, \langle \rho_b \rangle_V$ (see also Fig. 15). Including wall heat losses translates into a lower density ratio, which in turn yields a lower flame propagation speed and also a lower azimuthal flow acceleration. This can be examined in Fig. 23 showing the outflux of *fresh* gases $\dot{m}_u^{out}$ at the combustor outlet as a consequence of the burnt gas expansion. The time coordinate is rescaled such that the flame front merging is attained at $t/\tau^{\text{merging}} = 1$ (diamond markers in Fig. 13). Two key differences can be observed between both cases: first, the initial peak value of fresh gas outflux is larger in the adiabatic case than in the baseline case.

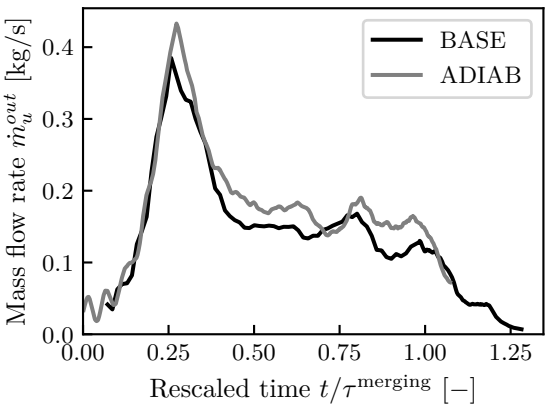

Figure 23: Mass flow rates of fresh gases $\dot{m}_u^{out}$ leaving the combustion chamber upstream of the propagating flame fronts. The time coordinate is rescaled by the respective flame front merging time τ^{merging} for each case.

Second, and more importantly, the adiabatic case can also sustain a higher level of fresh gas outflux almost throughout the entire light-round duration. Thus, the higher the density ratio, the higher the fresh gas mass flow rate and the azimuthal flow acceleration. Recalling that the flame propagates approximately at the speed of the accelerated flow [28], it can be inferred from the plot that flame propagation is generally faster when burnt gases are not subjected to wall heat losses.

Remarkably, S_a^T does not increase by the same amount as does the density ratio in Fig. 15 for example when passing form the baseline setup to an adiabatic setup. This behavior is attributed to the fact that the flame propagation speed is certainly not decoupled from Term II containing not only the burnt gas density $\langle \rho_b \rangle_V$, but also the *burnt* gas mass flow rate at the combustor outlet $\dot{m}_b^{out}$. When the flow acceleration through burnt gas ex-

pansion is more pronounced (*i.e.* when all walls are adiabatic), the outflux of burnt gases increases, which counterbalances the increase of Term I through an increased Term II as already seen in Fig. 18 (comparing dash-dotted lines for both cases). Therefore, the change of the density ratio does not control the resulting flame propagation speed *alone*.

Beyond the density ratio and outflux of burnt gases, other phenomena have to be considered as well. While the laminar flame speed S_l is essentially the same for both cases (see Fig. 20), as it is controlled primarily by the liquid phase, turbulence levels may be enhanced by a higher azimuthal velocity and increase the flame surface wrinkling. Consequently, all effects on the flame propagation speed have to be taken into account at the same time, since changes in one phenomenon are prone to affecting another. To corroborate this argument, flame/turbulence interactions are briefly covered in the next section, since a dedicated study on that subject is already published in [34].

5.2.3. Flame/Turbulence interactions

The resolved flame surface wrinkling $\Xi_{res} = A_{res}/A_0$ can be examined in Fig. 24 (solid and dashed lines) to prove the interaction between the volumetric burnt gas expansion and turbulence. The grayed area masks the first phase of light-round, where Eq. 15 cannot be applied.

For both cases, the evolution of the resolved flame surface wrinkling Ξ_{res} is similar, but case ADIAB exhibits higher values almost throughout the entire light-round. Up to the first peak, Ξ_{res} is on average 25% larger in the adiabatic case at a given instant, and still 15% larger between $t = 30\,\mathrm{ms}$ and $t = 45\,\mathrm{ms}$ compared to the baseline case. This contributes entirely to a larger Term I in the model expression for S_a^T and thus to the higher absolute

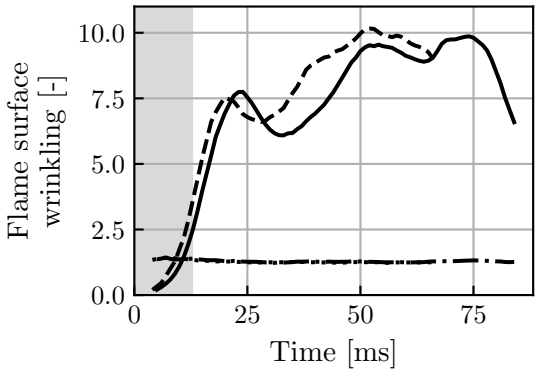

Figure 24: Resolved flame surface wrinkling Ξ_{res} for case BASE (solid line) and ADIAB (dashed line). The sub-grid scale flame surface wrinkling $\langle \Xi_{\Delta} \rangle_{res}$ averaged over the resolved surface is virtually the same for both cases (dash-dotted and dotted lines).

turbulent flame speed observed in the absence of wall heat losses.

Unlike the resolved flame surface wrinkling, the sub-grid scale flame surface wrinkling $\langle \Xi_{\Delta} \rangle_{res}$ averaged over the resolved flame surface is virtually the same for both cases (dash-dotted and dotted lines), and similar to the one examined in [34]. Due to identical computational meshes for both cases, identical values for the laminar flame thickness ($\delta_l \propto \phi$), and ϕ unchanged, very similar values can be observed for $\langle \Xi_{\Delta} \rangle_{res}$ (see Eq. 7) as well. In spite of a moderately higher flow acceleration during burnt gas expansion in the adiabatic case, a potentially higher turbulence intensity does not affect the sub-grid scale flame surface wrinkling in its *saturated* formulation. Therefore, with a similar flame surface wrinkling parameter β (not shown for brevity), a similar evolution of $\langle \Xi_{\Delta} \rangle_{res}$ can be expected.

5.3. Model sensitivities

With the insights of the previous model decomposition, the last goal of this work can finally be addressed. Changes are introduced separately to the model expression for S_a^T in Eq. 15 in the following way for otherwise unchanged variables:

- instead of a dynamic evaluation of the wrinkling parameter β, a constant value of $\beta \equiv 0.5$ is assumed and S_a^T is recomputed accordingly from the model expression showcasing a different modeling approach of flame/turbulence interactions;
- a constant laminar flame speed at the global equivalence ratio $S_l = S_l^0(\phi_{glob})$ is imposed instead of a flame surface averaged value addressing flame/droplet interactions and the role of the liquid phase in general;
- S_a^T is computed by setting Term III (temporal density variations) to zero to emulate a quasi-steady state;
- instead of variable values for the density ratio $\langle \rho_u \rangle_V \,/\, \langle \rho_b \rangle_V$, the corresponding values under nominal conditions are used to recompute the flame propagation speed targeting changes in the modeling of wall heat transfers.

While the analysis has outlined the relation between the different mechanisms, each of these changes is deliberately chosen to aim at one physical phenomenon at a time in order to estimate *a priori* a new value for S_a^T. Compared to the (unaltered) baseline simulation case, these new values for the flame propagation speed can then give an indication about the relative importance of each phenomenon. Such an *a priori* sensitivity study

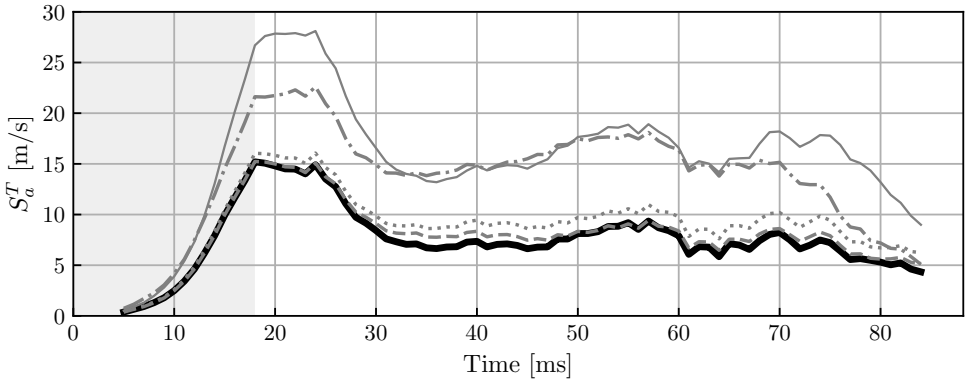

Figure 25: Impact of modeling choices: (▬): S_a^T of baseline case; (——): S_a^T for $\beta \equiv 0.5$; (-·-·-): S_a^T for $S_l = S_l^0(\phi_{glob})$; (- - -): S_a^T with Term III set to zero; (·····): S_a^T for nominal density ratio.

allows to establish a common methodology to compare the underlying mechanisms. Complementary studies with *a posteriori* computations are further referenced, where available, to assess the bias of the *a priori* estimations.

The resulting flame propagation speed for all four cases listed above are plotted in Fig. 25 as grey lines. The baseline case is added for reference (solid black line).

Starting with a constant β formulation, it shows the most substantial impact on S_a^T. With an approximately 50% higher flame surface averaged sub-grid scale wrinkling factor $\langle \Xi_\Delta \rangle_{res}$, the resulting flame propagation speed is around two times higher than in the baseline case. Compared to a 20% increase of the flame propagation speed as published in Ref. [34] (*a posteriori*), this modification of Eq. 15 certainly overestimates the flame propagation speed, since the higher flow acceleration generated by a constant flame sur-

face wrinkling parameter is not counterbalanced by an increased outflux of burnt gases in Term II.

Next, imposing a constant flame speed $S_l = S_l^0(\phi_{glob})$ results still in an averaged 82% increase of the flame propagation speed. Such high values clearly neglect the effect on Term II, in addition to flame/droplet interactions (*e.g.,* droplet accumulations, lower gaseous equivalence ratio, see Sec. 4.4), which decelerate the propagating flame fronts.

As expected with deactivating Term III, S_a^T increases marginally (6% on average), since temporal density variations are shown to be comparably small (see Sec. 5.1). It should be emphasized that neglecting the last term of Eq. 15 is not equivalent to case ADIAB, because Terms I and II are intentionally left unchanged for the sake of this *a priori* estimation.

Finally, recomputing the absolute turbulent flame propagation speed based on the nominal density ratio yields a 19% higher flame propagation speed. Interestingly, the predicted *a priori* value ($S^T_{a,\,a\,priori} = 10.44\,\mathrm{m/s}$) matches the averaged *a posteriori* value (given in Sec. 5.1) obtained from case ADIAB quite well.

The main conclusion that can be drawn from these *a priori* estimations is the fact that all major governing mechanisms of flame propagation tend to substantially impact the resulting absolute turbulent flame speed. It also supports the argument that each of the underlying physical phenomena requires careful consideration in terms of the employed model approach in LES, since any unsubstantiated simplifications may yield incorrect values for S_a^T or cause hidden error cancellation at worst. Moreover, it justifies the modeling choices made for the baseline case in this work, which addresses all rele-

vant phenomena at once, following the recommendations of previous studies. However, the *a priori* study has revealed a certain bias in terms of the predicted values, which has to be taken into consideration when estimating the impact of any phenomenon solely from an *a priori* perspective.

6. Conclusions

The present work explores the driving mechanisms of flame propagation during light-round and the role of physical modeling. Large-Eddy Simulations are performed in MICCA-Spray, an annular swirled spray-flame combustor with 16 fuel injectors fed by liquid n-heptane. Simulations are carried out with cold combustor walls at $T_w = 300\,\mathrm{K}$, allowing to assess the effect of wall heat transfer on flame propagation. Such conditions are highly relevant for flame propagation in confined multi-burner configurations, since a strong sensitivity to wall temperatures is observed in the available experimental data. Yet this relationship has not been thoroughly investigated. In a broader context, the role of physical models required to perform LES of light-rounds is analyzed. Specifically, the need for detailed models for the main governing mechanisms is highlighted.

The numerical setup follows previous works in terms of a dynamic closure for subgrid-scale flame surface wrinkling in the TFLES framework, polydisperse Lagrangian particle tracking, fuel injection and droplet evaporation. A tabulation approach is proposed for the wall model in order to overcome the limitations of standard logarithmic wall models and is capable of accounting for all variable properties in the boundary layer. Unlike previous related works that have concentrated on a single aspect at a time to isolate its effect

on flame propagation (heat losses, two-phase flow and dynamic combustion modeling) without addressing the other aspects, the current work attempts to incorporate the prior findings in a single numerical setup in order to draw general conclusions with respect to the impact of each model. Moreover, error cancellation can be avoided through this procedure as outlined by Puggelli et al. [34].

The predicted light-round duration is found to be in fairly good agreement with available experimental data for cold-wall conditions, in particular when considering the uncertainties associated with the synchronization procedure. The volumetric expansion of burnt gases induces an azimuthal flow acceleration as primary driving mechanism of flame propagation. It also acts on the liquid phase by creating a heterogeneous droplet distribution upstream of the flame fronts: droplets accumulate in the wake of the swirled jets, which in turn affects the trajectory of the flame. A characteristic sawtooth trajectory is observed for the leading point. Another consequence of the presence of liquid fuel is a diminished laminar flame speed S_l.

Furthermore, cold combustor walls also enhance the effect of heat losses on burnt gases, which are predominantly found further downstream in the burnt gas region, while the propagating flame fronts encounter almost adiabatic conditions. As a consequence, the burnt gas density increases and leads to a lower flame propagation speed compared to light-round ignition with adiabatic walls. The lack of experimental data currently precludes further assessment of heat losses, in particular their impact on flame stabilization mechanisms at $T_w = 300\,\mathrm{K}$ and atmospheric conditions. Such investigations could be considered in the future.

The flame surface wrinkling parameter β is briefly examined and shows a heterogeneous distribution consistent with previous research (low values across the propagating flame fronts versus higher values at the stabilized flames). The use of a dynamic evolution of the wrinkling parameter must therefore be preferred as no universal value exists which would result in the same flame surface wrinkling and thus the same flame propagation speed.

The second part of this study is concerned with a mathematical expression to model the absolute turbulent flame propagation speed during light-round and accurately predicts averaged values for both cases under consideration (baseline and adiabatic). The equation is decomposed to study the governing mechanisms in detail and relate them to the identified terms in the model equation. Lastly, the expression for turbulent flame propagation is modified to estimate from an *a priori* perspective to what extent the absolute turbulent flame speed may change with different modeling choices.

The study, which assembles various models for dynamic flame wrinkling, polydisperse spray description and wall heat losses, shows that neither corresponding physical mechanism outweighs the other ones and underscores the argument that each physical phenomenon must be accurately modeled. Variations in other modeling components have not been considered such as chemistry or subgrid-scale fluxes and could be investigated in future works. More specifically, local unsteady strain effects would certainly deserve a dedicated investigation in future works with better models to quantify their impact on the predicted flame speeds. Beyond light-round, we also expect strain corrections to better represent the very first instants of the initial stage of ignition which is only briefly covered on purpose.

Moreover, pre-heating combustor walls can presumably alleviate the characteristic sawtooth trajectory of the leading point by enhanced droplet evaporation, which may explain shorter light-round durations observed experimentally. This aspect is the subject of ongoing research.

Acknowledgments

This project has received funding from the European Union's Horizon 2020 research and innovation program [grant number 765998] (ANNULIGHT). HPC resources of the GENCI allocations [grant numbers A0082B10118, A0082B10159] and the Mésocentre computing cluster of CentraleSupélec and École Normale Supérieure Paris-Saclay supported by CNRS and Région Île-de-France are gratefully acknowledged. The authors would like to show their gratitude to Dr. G. Vignat, Dr. D. Durox and Prof. S. Candel for the fruitful discussions and performing detailed experimental measurements of the droplet spray used for calibration in this work. We would also like to thank Prof. D. Veynante for sharing his unparalleled knowledge and his invaluable advice on the subject of dynamic combustion modeling. The assistance provided by Dr. E. Riber and Dr. B. Cuenot from CERFACS with the initial Euler-Lagrange setup in AVBP is greatly appreciated.

Appendix A Thickened Flame LES in the context of multi-regime combustion

In the present work, we apply the TFLES model [31] initially developed for purely premixed combustion. In the general context of multi-regime (or

mixed-mode) combustion, however, heat release may be due to coexisting diffusion and premixed flames [75] for which a single-mode combustion model would be considered as a poor modeling choice, at least without *a priori* knowledge of the dominant combustion regime. As the MICCA-Spray combustor is operated with liquid fuels, it is conceivable that premixed and diffusion regimes may occur simultaneously due to flow inhomogeneities induced *e.g.,* by the liquid phase. Yet, the thickened flame combustion model can still be justified for our setup, mainly due to the following two reasons:

1. n-heptane is a volatile fuel even under ambient conditions which aids evaporation and fuel/air mixing.

2. *A priori* knowledge exists originating from earlier studies of light-round in two-phase flows [34] suggesting that combustion predominantly takes place in the premixed combustion regime.

We also provide an *a posteriori* verification of our assumptions in Fig. A1 showing a map of the Takeno flame index [58] on the central unwrapped cutplane at $R = 0.175\,\mathrm{m}$ used throughout this work. By convention, the flame index takes values of $+1$ in the premixed combustion regime (shaded in red in Fig. A1) and -1 in the diffusion regime (shaded in blue). The time instant of $t = 41\,\mathrm{ms}$ is counted from $t_0 = 0\,\mathrm{ms}$ (flame kernel delivered in the outer recirculation zone of the first burner, cf. Sec. 4.1) and the flame fronts are propagating from the sides to the center of this unwrapped image. The instantaneous position of the reaction zones are given by iso-contours of the heat release rate (HRR). These are found to be located in the premixed combustion zone, justifying the use of the thickened flame model for the

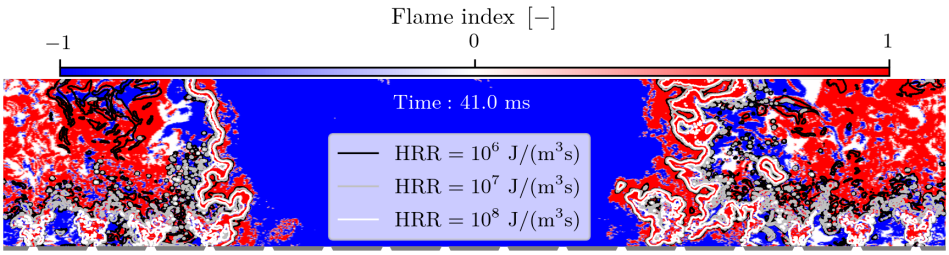

Figure A1: Takeno flame index [58] on an unwrapped cylindrical cut-plane at $R = 0.175\,\mathrm{m}$. Red zones indicate a premixed combustion regime, while blue zones indicate a diffusion regime. The instantaneous position of the reaction zone is given by iso-contours of the heat release rate (HRR).

present case.

The identification of premixed combustion zones then allows to artificially thicken the premixed reaction zone by applying a flame sensor [32]. We recall the definition of the sensor function as

$$\theta_F \doteq \tanh\left(\beta \frac{\Omega}{\Omega_0}\right) \tag{18}$$

where Ω is an "Arrhenius-like expression" given as

$$\Omega = Y_F^{\nu_F} Y_O^{\nu_O} \exp\left(-\Gamma \frac{T_a}{T}\right) \tag{19}$$

and Ω_0 is its maximum value tabulated as a function of the local equivalence ratio. The calibration parameter β in Eq. 18 is set to 50, and the activation coefficient Γ in Eq. 19 is set to 0.5 consistently with Ref. [32]. Fuel and oxidizer mass fractions are denoted as Y_F and Y_O, respectively and ν_F and ν_O correspond to their stoichiometric reaction coefficients. The activation energy for the first reaction of the two-step reaction mechanism [55] is $T_a = 14\,593\,\mathrm{K}$ and T is the local temperature.

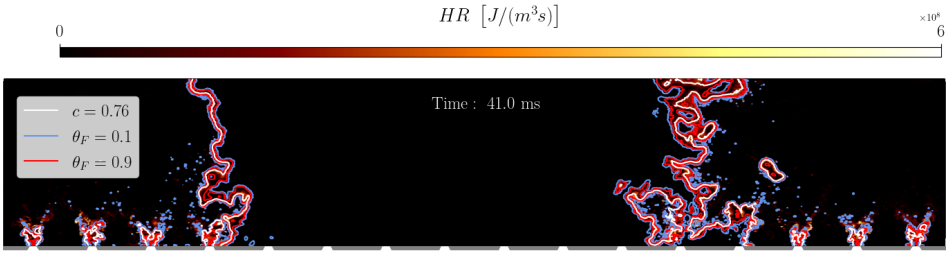

Figure A2: Instantaneous heat release rate on an unwrapped cylindrical cut-plane at $R = 0.175\,\mathrm{m}$. Iso-contours of the progress variable $c = 0.76$ (at peak heat release) are included as white lines which are surrounded by red contour lines marking the region where the flame sensor is active. Blue contour lines indicate the direction in which the sensor function θ_F decreases.

This mathematical framework allows the detection of the reaction zone where $\theta_F = 1$, and $\theta_F = 0$ elsewhere in the domain, *i.e.* outside of the reaction zone. As we show in Fig. A2, the white iso-contour of the progress variable $c = 0.76$ (corresponding to the peak of the fuel species source term) lies in-between the active region of the flame sensor marked by red contour lines, proving the correct functioning of the sensor. Blue contour lines are added to indicate the direction in which the sensor function θ_F decreases.

With an imposed resolution of $n = 7$ grid points across the reaction zone the local amount of thickening can eventually be determined as

$$F = 1 + (F_{\max} - 1) \underbrace{\tanh\left(\beta \frac{\Omega}{\Omega_0}\right)}_{\theta_F} \tag{20}$$

where the maximum required thickening $F_{\max}$ follows from the local laminar flame thickness δ_l^0 (tabulated as a function of local the equivalence ratio),

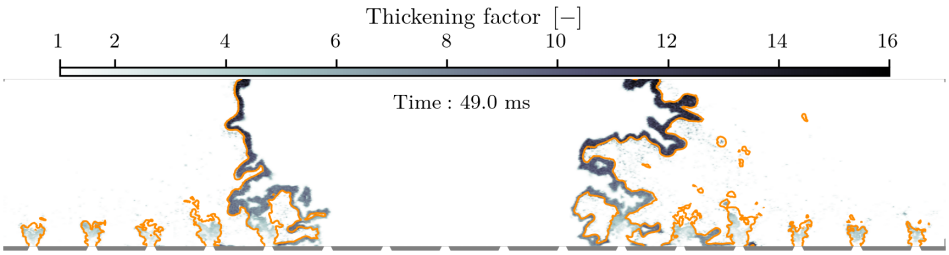

Figure A3: Local thickening factor F on an unwrapped cylindrical cut-plane at $R = 0.175\,\mathrm{m}$. Contour lines correspond to a progress variable value of $c = 0.76$.

the local cell size Δ and the requested number of grid points n

$$F_{\max} = \frac{n\,\Delta}{\delta_l^0} \tag{21}$$

Typical values of F are comparably low closer to the chamber backplane ($F \lesssim 4$) and may be higher towards the combustor outlet ($F \approx 20$) as visualized in Fig. A3.

Appendix B Impact of wall model formulation on wall heat fluxes

Similar to the comparison in Puggelli et al. [24] we compare the predicted wall heat fluxes of our baseline case with recomputed heat fluxes obtained from a classical logarithmic wall model. Due to substantial temperature variations in the boundary layer, its thermophysical properties (ρ, μ, c_p λ) necessarily have to change as well and thus critically affect the resulting wall heat fluxes [24]. To prove to what extent the amount of wall heat fluxes would change, if instead of variable thermophysical properties (as in our baseline case) only the boundary layer density was allowed to change, we compare the wall heat fluxes across the inner combustor wall with two different wall models in Fig. B4. In both images, negative values correspond to a (directional)

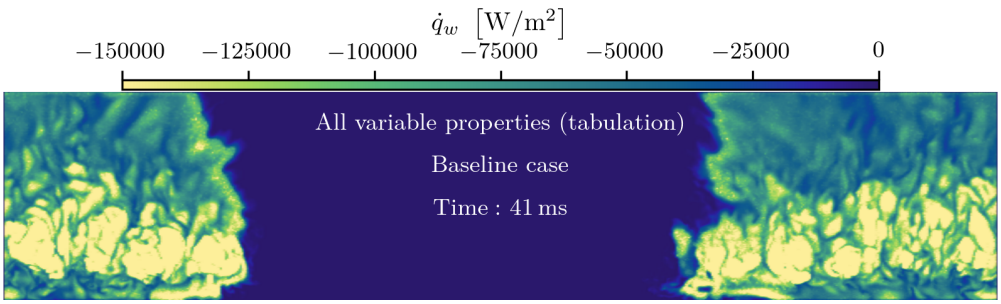

(a)

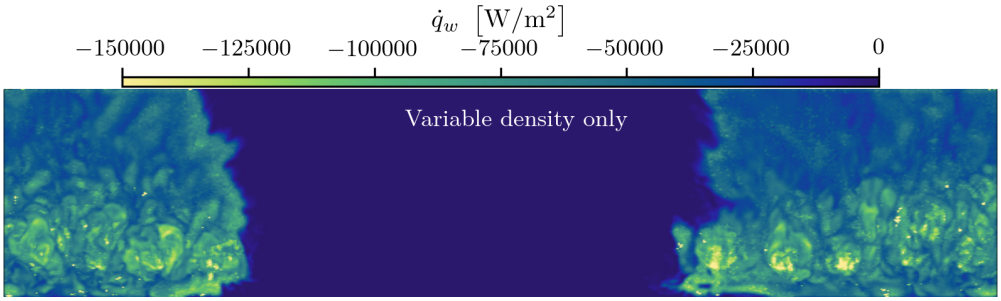

(b)

Figure B4: Comparison of wall heat fluxes across the inner combustor wall for two different wall models: a) corresponds to the baseline case where all thermophysical properties are variable (ρ, μ, c_p λ). In b) the wall heat flux is recomputed allowing only the boundary layer density to change.

heat flux from the fluid onto the combustor wall. Figure B4(a) represents the baseline case of the present work and exhibits substantial heat fluxes in the vicinity of stabilized flames where flow velocities are comparably high due to the swirling jets emerging from each injector. Heat fluxes are slightly less pronounced in the upper half of the combustor due to a lowered burnt gas velocity. In the fresh gas region at the center, heat fluxes are essentially zero, since fresh gases injected at $T = 300\,\mathrm{K}$ are at the same temperature as the combustor wall. In turn, the recomputed wall heat fluxes predicted by a classical logarithmic wall model and variable boundary layer density only are greatly diminished across the entire burnt gas region (Fig. B4(b)), clearly illustrating the importance of accounting for variable thermophysical boundary layer properties.

References

[1] A. H. Lefebvre, D. R. Ballal, Gas Turbine Combustion: Alternative Fuels and Emissions, CRC Press, Boca Raton, Florida, USA, 2010.

[2] E. Mastorakos, Forced ignition of turbulent spray flames, Proc. Combust. Inst. 36 (2017) 2367–2383.

[3] M. Cordier, A. Vandel, B. Renou, G. Cabot, M. A. Boukhalfa, L. Esclapez, D. Barré, E. Riber, B. Cuenot, L. Gicquel, Experimental and Numerical Analysis of an Ignition Sequence in a Multiple-Injectors Burner, Proceedings of the ASME Turbo Expo 2013: Turbine Technical Conference and Exposition 1A (2013).

[4] D. Barré, L. Esclapez, M. Cordier, E. Riber, B. Cuenot, G. Staffelbach,

B. Renou, A. Vandel, L. Y. Gicquel, G. Cabot, Flame propagation in aeronautical swirled multi-burners: Experimental and numerical investigation, Combust. Flame 161 (2014) 2387–2405.

[5] E. Machover, E. Mastorakos, Experimental and numerical investigation on spark ignition of linearly arranged non-premixed swirling burners, Combust. Sci. Technol. 189 (2017) 1326–1353.

[6] J. Marrero-Santiago, A. Verdier, C. Brunet, A. Vandel, G. Godard, G. Cabot, M. Boukhalfa, B. Renou, Experimental Study of Aeronautical Ignition in a Swirled Confined Jet-Spray Burner, J. Eng. Gas Turb. Power 140 (2017).

[7] J. Marrero-Santiago, A. Verdier, A. Vandel, G. Cabot, A. M. Boukhalfa, B. Renou, Effect of injector spacing in the light-around ignition efficiency and mechanisms in a linear swirled spray burner, Heat Mass Transfer 55 (2019) 1871–1885.

[8] J. F. Bourgouin, D. Durox, T. Schuller, J. Beaunier, S. Candel, Ignition dynamics of an annular combustor equipped with multiple swirling injectors, Combust. Flame 160 (2013) 1398–1413.

[9] E. Machover, E. Mastorakos, Experimental investigation on spark ignition of annular premixed combustors, Combust. Flame 178 (2017) 148–157.

[10] Y. Xia, C. Linghu, Y. Zheng, C. Ye, C. Ma, H. Ge, G. Wang, Experimental Investigation of the Flame Front Propagation Characteristic

During Light-round Ignition in an Annular Combustor, Flow Turbul. Combust. (2019) 247–269.

[11] W. Gao, J. Yang, F. Liu, Y. Mu, C. Liu, G. Xu, Experimental investigation on the flame propagation pattern of a staged partially premixed annular combustor, Combust. Flame 230 (2021) 111445.

[12] E. Bach, J. Kariuki, J. R. Dawson, E. Mastorakos, H. J. Bauer, Spark ignition of single bluff-body premixed flames and annular combustors, 51st AIAA Aerospace Sciences Meeting including the New Horizons Forum and Aerospace Exposition (2013), paper AIAA 2013-1182.

[13] Y.-H. Kao, M. Denton, X. Wang, S.-M. Jeng, M.-C. Lai, Experimental Spray Structure and Combustion of a Linearly-Arranged 5-Swirler Array, Proceedings of the ASME Turbo Expo 2015: Turbine Technical Conference and Exposition (2015), paper GT2015-42509.

[14] M. Philip, M. Boileau, R. Vicquelin, T. Schmitt, D. Durox, J. F. Bourgouin, S. Candel, Simulation of the ignition process in an annular multiple-injector combustor and comparison with experiments, J. Eng. Gas Turb. Power 137 (2015).

[15] R. Ciardiello, P. M. de Oliveira, A. W. Skiba, E. Mastorakos, P. M. Allison, Effect of spark location and laminar flame speed on the ignition transient of a premixed annular combustor, Combust. Flame 221 (2020) 296–310.

[16] E. Machover, E. Mastorakos, Spark ignition of annular non-premixed combustors, Exp. Therm. Fluid Sci. 73 (2016) 64–70.

[17] C. Ye, G. Wang, Y. Fang, C. Ma, L. Zhong, S. Moreau, Ignition dynamics in an annular combustor with gyratory flow motion, Proceedings of the ASME Turbo Expo 2018: Turbomachinery Technical Conference and Exposition (2018), paper GT2018-76624.

[18] D. Ballal, A. Lefebvre, Flame propagation in heterogeneous mixtures of fuel droplets, fuel vapor and air, Symp. (Int.) Combust. 18 (1981) 321–328.

[19] A. Neophytou, E. Mastorakos, Simulations of laminar flame propagation in droplet mists, Combust. Flame 156 (2009) 1627–1640.

[20] P. M. de Oliveira, E. Mastorakos, Mechanisms of flame propagation in jet fuel sprays as revealed by OH/fuel planar laser-induced fluorescence and OH* chemiluminescence, Combust. Flame 206 (2019) 308–321.

[21] K. Prieur, D. Durox, J. Beaunier, T. Schuller, S. Candel, Ignition dynamics in an annular combustor for liquid spray and premixed gaseous injection, Proc. Combust. Inst. 36 (2017) 3717–3724.

[22] D. H. Wacks, N. Chakraborty, E. Mastorakos, Statistical Analysis of Turbulent Flame-Droplet Interaction: A Direct Numerical Simulation Study, Flow Turbul. Combust. 96 (2016) 573–607.

[23] D. H. Wacks, N. Chakraborty, Flame Structure and Propagation in Turbulent Flame-Droplet Interaction: A Direct Numerical Simulation Analysis, Flow Turbul. Combust. 96 (2016) 1053–1081.

[24] S. Puggelli, T. Lancien, K. Prieur, D. Durox, S. Candel, R. Vicquelin, Impact of Wall Temperature in Large Eddy Simulation of Light-Round

in an Annular Liquid Fueled Combustor and Assessment of Wall Models, J. Eng. Gas Turb. Power 142 (2020) 1–11.

[25] M. Boileau, G. Staffelbach, B. Cuenot, T. Poinsot, C. Bérat, LES of an ignition sequence in a gas turbine engine, Combust. Flame 154 (2008) 2–22.

[26] M. Philip, M. Boileau, R. Vicquelin, E. Riber, T. Schmitt, B. Cuenot, D. Durox, S. Candel, Large Eddy Simulations of the ignition sequence of an annular multiple-injector combustor, Proc. Combust. Inst. 35 (2015) 3159–3166.

[27] W. Zhao, L. Zhou, W. Qin, H. Wei, Large Eddy Simulation of Multiple-Stage Ignition Process of n-Heptane Spray Flame, J. Eng. Gas Turb. Power 141 (2019) 1–12.

[28] T. Lancien, K. Prieur, D. Durox, S. Candel, R. Vicquelin, Large Eddy Simulation of Light-Round in an Annular Combustor With Liquid Spray Injection and Comparison With Experiments, J. Eng. Gas Turb. Power 140 (2017).

[29] F. Collin-Bastiani, Modeling and Large Eddy Simulation of Two-Phase Ignition in Gas Turbines, Ph.D. thesis, Institut National Polytechnique de Toulouse, France, 2019.

[30] T. Lancien, K. Prieur, D. Durox, S. Candel, R. Vicquelin, Leading point behavior during the ignition of an annular combustor with liquid n-heptane injectors, Proc. Combust. Inst. 37 (2019) 5021–5029.

[31] O. Colin, F. Ducros, D. Veynante, T. Poinsot, A thickened flame model for large eddy simulations of turbulent premixed combustion, Phys. Fluids 12 (2000) 1843–1863.

[32] J. P. Legier, T. Poinsot, D. Veynante, Dynamically thickened flame LES model for premixed and non-premixed turbulent combustion, Proc. CTR Summer Program (2000) 157–168.

[33] B. Fiorina, R. Vicquelin, P. Auzillon, N. Darabiha, O. Gicquel, D. Veynante, A filtered tabulated chemistry model for LES of premixed combustion, Combust. Flame 157 (2010) 465–475.

[34] S. Puggelli, D. Veynante, R. Vicquelin, Impact of dynamic modelling of the flame subgrid scale wrinkling in large-Eddy simulation of light-round in an annular combustor, Combust. Flame 230 (2021) 111416.

[35] R. W. Read, J. W. Rogerson, S. Hochgreb, Relight imaging at low temperature, Low pressure conditions, 46th AIAA Aerospace Sciences Meeting and Exhibit (2008) 1–13.

[36] T. Mosbach, R. Sadanandan, W. Meier, R. Eggels, Experimental analysis of altitude relight under realistic conditions using laser and high-speed video techniques, Proceedings of the ASME Turbo Expo 2 (2010) 523–532.

[37] M. J. Denton, S. B. Tambe, S. M. Jeng, Experimental investigation into the high altitude relight of a three-cup combustor sector, Proceedings of the ASME Turbo Expo 4B (2018) 1–12.

[38] A. D. Martinos, N. Zarzalis, S. R. Harth, Analysis of ignition processes at combustors for aero engines at high altitude conditions with and without effusion cooling, Proceedings of the ASME Turbo Expo 1 (2020) 1–10.

[39] H. Klinger, S. Bake, H. F. Vogt, D. Knieschke, P. Schober, Altitude testing of the E3E core engine, Proceedings of the ASME Turbo Expo 1 (2011) 223–232.

[40] K. Prieur, G. Vignat, D. Durox, T. Schuller, S. Candel, Flame and spray dynamics during the light-round process in an annular system equipped with multiple swirl spray injectors, J. Eng. Gas Turb. Power 141 (2019).

[41] T. Schönfeld, M. Rudgyard, Steady and Unsteady Flow Simulations Using the Hybrid Flow Solver AVBP, AIAA J. 37 (1999) 1378–1385.

[42] O. Colin, M. Rudgyard, Development of High-Order Taylor-Galerkin Schemes for LES, J. Comput. Phys. 162 (2000) 338–371.

[43] F. Nicoud, H. B. Toda, O. Cabrit, S. Bose, J. Lee, Using singular values to build a subgrid-scale model for large eddy simulations, Phys. Fluids 23 (2011).

[44] L. Schiller, A. Naumann, A drag coefficient correlation, Z. Ver. Dtsch. Ing. 77 (1935) 318–320.

[45] D. B. Spalding, The combustion of liquid fuels, Symp. (Int.) Combust. 4 (1953) 847–864.

[46] B. Abramzon, W. A. Sirignano, Droplet vaporisation model for spray combustion calculations, Int. J. Heat Mass Tran. 32 (1989) 1605–1618.

[47] N. Frössling, Über die Verdunstung fallender Tropfen (On the evaporation of falling drops), Gerl. Beitr. Geophys. 52 (1938) 170–216.

[48] G. L. Hubbard, V. E. Denny, A. F. Mills, Droplet Evaporation: Effects of Transients and Variable Properties, Int. J. Heat Mass Tran. 18 (1975) 1003–1008.

[49] K. Töpperwien, F. Collin-Bastiani, E. Riber, B. Cuenot, G. Vignat, K. Prieur, D. Durox, S. Candel, R. Vicquelin, Large-Eddy Simulation of Flame Dynamics During the Ignition of a Swirling Injector Unit and Comparison With Experiments, J. Eng. Gas Turb. Power 143 (2021).

[50] P. Jenny, D. Roekaerts, N. Beishuizen, Modeling of turbulent dilute spray combustion, Prog. Energ. Combust. 38 (2012) 846–887.

[51] A. R. Masri, Turbulent Combustion of Sprays: From Dilute to Dense, Combust. Sci. Technol. 188 (2016) 1619–1639.

[52] M. Sanjosé, J. M. Senoner, F. Jaegle, B. Cuenot, S. Moreau, T. Poinsot, Fuel injection model for Euler-Euler and Euler-Lagrange large-eddy simulations of an evaporating spray inside an aeronautical combustor, Int. J. Multiphas. Flow 37 (2011) 514–529.

[53] G. Vignat, P. Rajendram Soundararajan, D. Durox, A. Vié, A. Renaud, S. Candel, A Joint Experimental and LES Characterization of the Liquid Fuel Spray in a Swirl Injector, J. Eng. Gas Turb. Power (2021).

[54] C. Chauveau, M. Birouk, F. Halter, I. Gökalp, An analysis of the droplet support fiber effect on the evaporation process, Int. J. Heat Mass Tran. 128 (2019) 885–891.

[55] D. Paulhiac, B. Cuenot, E. Riber, L. Esclapez, S. Richard, Analysis of the spray flame structure in a lab-scale burner using Large Eddy Simulation and Discrete Particle Simulation, Combust. Flame 212 (2020) 25–38.

[56] B. Franzelli, E. Riber, M. Sanjosé, T. Poinsot, A two-step chemical scheme for kerosene-air premixed flames, Combust. Flame 157 (2010) 1364–1373.

[57] A. J. Smallbone, W. Liu, C. K. Law, X. Q. You, H. Wang, Experimental and modeling study of laminar flame speed and non-premixed counterflow ignition of n-heptane, Proc. Combust. Inst. 32 (2009) 1245–1252.

[58] H. Yamashita, M. Shimada, T. Takeno, A numerical study on flame stability at the transition point of jet diffusion flames, Symp. (Int.) Combust. 26 (1996) 27–34.

[59] S. Popp, G. Kuenne, J. Janicka, C. Hasse, An extended artificial thickening approach for strained premixed flames, Combust. Flame 206 (2019) 252–265.

[60] F. Charlette, C. Meneveau, D. Veynante, A power-law flame wrinkling model for LES of premixed turbulent combustion Part II: Dynamic formulation, Combust. Flame 131 (2002) 181–197.

[61] S. Mouriaux, O. Colin, D. Veynante, Adaptation of a dynamic wrinkling model to an engine configuration, Proc. Combust. Inst. 36 (2017) 3415–3422.

[62] O. Cabrit, F. Nicoud, Direct simulations for wall modeling of multicomponent reacting compressible turbulent flows, Phys. Fluids 21 (2009) 0–29.

[63] N. Maheu, V. Moureau, P. Domingo, F. Duchaine, G. Balarac, Large-Eddy Simulations and of flow and heat transfer and around a low-Mach number turbine blade, Proc. CTR Summer Program (2012) 137–146.

[64] H. Schlichting, K. Gersten, Boundary-Layer Theory, Springer, Berlin, Heidelberg, 2017.

[65] W. Cabot, P. Moin, Approximate wall boundary conditions in the large-eddy simulation of high Reynolds number flow, Flow Turbul. Combust. 63 (2000) 269–291.

[66] P. G. Huang, G. N. Coleman, P. Bradshaw, Compressible turbulent channel flows: DNS results and modelling, J. Fluid Mech. 305 (1995) 185–218.

[67] A. Patel, J. W. Peeters, B. J. Boersma, R. Pecnik, Semi-local scaling and turbulence modulation in variable property turbulent channel flows, Phys. Fluids 27 (2015).

[68] W. M. Kays, Turbulent Prandtl Number—Where Are We?, J. Heat Transf. 116 (1994) 284–295.

[69] T. Poinsot, S. Lele, Boundary conditions for direct simulations of compressible viscous flows, J. Comput. Phys. 101 (1992) 104–129.

[70] Corning Inc., Corning HPFS 7979, 7980, 8652, 8655 Fused Silica Optical Materials Product Information, Technical Report, Corning Inc., 2015.

[71] G. Chaussonnet, O. Vermorel, E. Riber, B. Cuenot, A new phenomenological model to predict drop size distribution in Large-Eddy Simulations of airblast atomizers, Int. J. Multiphas. Flow 80 (2016) 29–42.

[72] M. Philip, Dynamics of light-round in multi-injector annular combustors, Ph.D. thesis, Université Paris-Saclay, France, 2016.

[73] D. Veynante, L. Vervisch, Turbulent combustion modeling, Prog. Energ. Combust. 28 (2002) 193–266.

[74] B. Rochette, E. Riber, B. Cuenot, Effect of non-zero relative velocity on the flame speed of two-phase laminar flames, Proc. Combust. Inst. 37 (2019) 3393–3400.

[75] A. R. Masri, Challenges for turbulent combustion, Proc. Combust. Inst. 38 (2021) 121–155.